APPLICATION OF CASCADE THEORIES TO AXIAL FLOW PUMPS

Thesis by

Hans D. Linhardt
Diplom- Ing. Technische - Hochschule München

In Partial Fulfillment of the Requirements
For the Degree of
Mechanical Engineer

California Institute of Technology
Pasadena, California
1960

ABSTRACT

It is demonstrated with experiments and theory that the performance of an axial flow pump can be described very accurately by application of two-dimensional cascade theories including the thickness effect of the blades on the flow. The blade thickness is found to be an important parameter which is mainly responsible for discrepancies between the experimental results and predictions of "thin-airfoil" cascade theories. Three-dimensional effects and the effect of the boundary-displacement thickness on the cascade flow are shown to be negligible for the case of the axial flow pump of high stagger angle and low aspect ratio, which was the case for the present work.

ACKNOWLEDGEMENTS

The writer wishes to express his deepest appreciation to Dr. A. J. Acosta, who not only initiated the research program, but whose interest, suggestions, and criticisms were instrumental in its completion.

The constant cooperation and many-faceted skills of Mr. Jack R. Kingan were invaluable in conducting the experiments.

Many thanks are extended to the staff of the Hydrodynamics Laboratory for assistance in the experimental work, as well as to Barbara Rickert, who typed the manuscript.

TABLE OF CONTENTS

APPLICATION OF CASCADE THEORIES TO AXIAL FLOW PUMPS

I. INTRODUCTION

This paper is concerned with the analysis of application of cascade theories to axial flow pumps. An axial flow pump, in its simplest form, has a cylindrical outer casing, in which an impeller consisting of a hub section with attached blades is mounted. The rotation of the impeller imparts energy to the axially approaching fluid. The flow through the blade system is usually analyzed in two steps. First, an effective axisymmetric meridian flow, which accounts for the radial shift of the stream-lines in the meridian plane, is determined. The influence of one blade upon another, flow turning and other physical effects are then treated on this cylindrical surface in the second step. Under some conditions the stream-line shift is small and it has been found possible to assume that the flow passes through the impeller on straight, circular cylindrical sections concentric with the casing. The flow in each of these cylindrical sections is then developed into a plane. The blade system appears in this plane as a two-dimensional lattice or cascade as shown in Fig. 1. The cascade is described by the ratio of the chord to the spacing, called solidity, and the angle, called the stagger angle, between the perpendicular to the chord and the cascade plane. All airfoils of the lattice are identical. The flow through a lattice of airfoils has been determined theoretically with the assumption that the flow is inviscid, incompressible and irrotational (1)*. The viscous effect may be estimated later by use of well known boundary-layer theory as outlined in references (2), (3), (4).

*Numbers in parentheses refer to the references at the end of the text.

The case of thin blades with a small camber ("shallow" mean line) is particularly susceptible to potential flow analysis. Theories of this kind are called "thin-airfoil theories". Among the first of such theories to achieve widespread use is that of Weining (5). He treated the case of a cascade of circular arc airfoils of zero thickness. Many papers have appeared in recent years on this subject, and among the most noteworthy may be mentioned the work of Traupel (6), Katzoff (7), Klingmann (8) and Rannie (9).

Cascade theories, when used in conjunction with estimates of the stream-line shift of the particular blade section considered, have resulted in successful design procedures and methods of analysis for high performance axial-flow compressors. An excellent comprehensive review of these problems is given in a recent series of NACA reports (10). However, it has been reported (11) that for certain types of axial flow pumps these procedures are inadequate. These pumps are characterized by low blade angle and a relatively small ratio of blade height to axial extent. Axial-flow water pumps usually have such geometries due to limitations of construction, motor speed and expense. As a result such devices as a rule have few blades of low blade angle (high stagger angle) with ratios of blade height to chord length of one half or less. In addition the low blade angles result in a machine operating at much lower flow coefficients (see notation Appendix I) than are typical for modern high-performance compressor stages. Thus, for such designs the range of typical performance parameters (i.e., head coefficient, flow coefficient) is significantly different from that experienced in the compressor field.

It is not uncommon in axial flow pump practice for one blade to subtend an arc of 60-70°. The small ratio of blade height to chord, with the axial projection of the blade frequently being equal to or exceeding the blade height results in an impeller of strikingly different appearance than a fan or compressor. In fact, the bladed aspect presented by so many axial flow-pump impellers is so pronounced that one wonders whether large deviations from the model of a two-dimensional cascade might occur. Considering this, some designers doubt whether two-dimensional cascade theories are even meaningful for axial flow pump designs (12). Yet again many axial-flow pumps have been designed by applying two-dimensional, isolated airfoil data in connection with certain empirical corrections (13), (14). Some of these methods produced fair designs but have not been satisfactory in certain cases of low aspect ratio and modest solidity as observed by Bowerman (11). In view of all these facts Bowerman made an attempt to establish theoretical corrections to the performance of isolated airfoil sections when subjected to the influence of the cylindrical boundaries of a pump. His method takes into account the interference effect of one helical blade upon another in the presence of a cylindrical hub and case. For this purpose the blades were replaced by several discrete, radial vortices of constant strength from hub to tip. An exact solution was obtained for a single vortex and the effect of a complete blade was built up in an approximate way by superposition. The effect of the blade thickness was neglected completely.

However, to determine the validity of his approximate theory, Bowerman designed a two-bladed test impeller of the free-vortex type

as shown in Fig. 2. The performance of the impeller was then evaluated by measuring the distribution of the static pressure on the blades using the method of (15), and these measurements were employed to determine lift coefficients. Since the test results seemed to agree very well with his interference theory, and showed rather severe deviations from thin air-foil theories, Bowerman concluded that two-dimensional cascade theories do not predict properly the performance of axial flow pumps. A strict comparison was only made at zero angle of attack since his design method was restricted to this value. It was found that the measured lift coefficients were about twenty to twenty five percent lower than the values determined by cascade theories for air-foils of zero thickness. These results are disturbing since much research has demonstrated overwhelmingly the accuracy and usefulness of the cascade approach, in connection with the boundary-layer concept, for predicting the performance of other turbo-machines.

The comparison of compressor and pump geometries, previously mentioned, reveals that the pump utilizes a smaller number of blades of moderate thickness, lower aspect ratio and higher stagger angles than a compressor. Preliminary comparison of rather sketchy results from a current cascade theory including the effect of blade thickness (16) indicated that this effect may be much more important for pump designs of the type described than a typical compressor design. Therefore, rather than abandon what has proved to be a fruitful design procedure for a difficult and tedious calculation of three-dimensional effects, it seems necessary to examine the possibility of blade-thickness and boundary-layer effects being responsible for the deviations quoted by Bowerman.

Thus, it appears desirable to reconsider in detail the performance of Bowerman's test impeller.

The objective of the experimental and theoretical program discussed herein will be outlined in the next section. A description of the test facilities and of the test procedure is then presented and the method of data reduction is explained thoroughly. The theoretical performance calculations follow and are compared with the experimental results. Finally the results of these investigations are reviewed critically and their use for practical application discussed.

II. OBJECTIVE OF MEASUREMENTS

The objective of the experimental program is to establish the cascade performance of Bowerman's impeller and to compare it with modern cascade theories. The performance of an airfoil isolated or in cascade is usually determined by dimensionless parameters called lift and drag coefficients. The lift coefficient is a criterion of the blade loading and the drag coefficient is a measure of the viscous losses. Both parameters are functions of the particular blade and cascade geometry and the angle of attack (defined as the angle between the mean relative vector velocity and the chord line). Of particular interest is the lift coefficient for zero angle of attack and the slope of the lift curve, since the lift coefficient is nearly a linear function of the angle of attack. The design point of Bowerman's impeller was for zero angle of attack. This was done with the expectation of superior cavitation performance due to the particular mean-line chosen. However, his method

did not enable him to predict the lift-slope curve and hence also the off-design performance of the impeller. Needless to say, it is of great importance to be able to determine off-design behaviour and for this purpose it is necessary to know the slope of the lift curve. An important feature of interest is to find out if the discrepancy at zero angle of attack previously mentioned extends also to the lift-slope curve.

To measure these quantities experimentally, it is necessary to make extremely accurate flow surveys upstream and downstream of the impeller at several different flow rates. Stream-line shifts, the lift and drag coefficients corresponding to each stream-line and the section lift slope as well as the cascade factor (the ratio of the lift-slope in the cascade to the isolated case) can then be calculated. The actual performance so found is then compared with several cascade theories including thickness and viscous effects.

Any type of axial-flow pump could have been used for the present study. However, because of the importance of this problem for the designer, it was believed best to use the same equipment Bowerman employed in his work in order to reduce the uncertainty in applying the results to his machine.

III. TEST EQUIPMENT

1. Impeller.

The details of the test impeller used by Bowerman are shown in Fig. 2, which is taken from (11). Briefly, Fig. 2 shows the test pump and its blade sections from hub to tip. The geometric parameters are also listed in this figure. It will be seen that the solidity is nearly constant

from root to tip with a value of about 0.716. The aspect ratio is $h/c^{*} = 0.556$ and the stagger angle of the mean section is $\gamma = 66.40^{\circ}$. The blade sections consist of symmetrical NACA 65 camber lines and NACA 16009 thickness functions. The thickness is scaled linearly from tip to hub. The isolated lift coefficient of the mean section is quoted by (11) to be $C_L = 0.604$ and the lift coefficient in the cascade is predicted to be $C_L = 0.558$. The design head coefficient amounts to $\psi_d = 0.126$ at the design flow rate $\varphi_d = 0.315$. The design flow rate occurs at the flow rate φ_i, indicated by the venturi meter at about $\varphi_i = 0.295$ as observed by Bowerman. This is due to some wall-boundary layer blockage. In the following the indicated flow rate φ_i is used for presentation of the measurements.

2. Test Facilities.

The experimental facilities of the rotating machinery laboratory of the California Institute of Technology have been discussed many times in Hydrodynamic Laboratory reports (15) and (11). Therefore, only a brief discussion will be given here.

The test impeller is driven by a dynamometer, which is speed-controlled and permits accurate torque measurements. The flow is supplied by a speed-controlled service pump and is measured by a venturi meter.

The pump installation deviates from that of (11) by several counts in so far as the rotating manometer was disconnected and that the discharge

---

* See notations in Appendix I at the end of the text.

section was extended by a plexiglas ring. The measuring station downstream was chosen at 2.5 in. axial distance from the trailing edge, where uniform-flow conditions can be expected. This station is located at (x/c) = 0.5 with respect to the absolute flow.

The measuring probes are attached to a probe holder, shown in Fig. 3, which is mounted on the outside of the test pit. A special joint was machined which allows the calibrated probe positions to match accurately the probe holder readings. The probe holder permits accurate angle and pressure readings for any radial position. The upstream station is taken at the same location as (11) reported. Three static pressure taps were located in this plane to provide an accurate reference point for all measurements. All pressure measurements were conducted with an 0.2 psi Statham strain gage in connection with a Baldwin, high precision amplifier and bridge circuit. The flow angles were determined with the same equipment.

3. Measuring Probes.

The flow angles are measured with a wedge probe as shown in Fig. 4a. The static pressure is recorded by a static pressure probe of such design that no disturbance is produced by the instrument itself. Fig. 4b shows the dimensions of the probe. The total pressure of the mean-flow passage η = 0.70 - 0.90 is measured with a ducted total pressure probe, known as Kiel probe (Fig. 4c). For all other positions a boundary-layer probe was employed for very accurate measurement of the total pressure near the casing and wall. The probe is shown in Fig. 4d.

4. Expected Measuring Errors.

Based on past experience, the error of the static pressure probe should be smaller than ± 1 percent, that of the total pressure probe about ± 1/2 percent and that of the angle or wedge probe on the order of ± 1/4 percent. These deviations are referred to two-dimensional flow surveys. In such a case the velocities should be measured accurately in the range of ± 0.75 percent. The lift coefficient should be close to ± 3 percent and $(dC_L/d\alpha)$ should be obtained with an accuracy of ± 3.72 percent in the case of a drag coefficient of the order $C_D = 0.008$. If higher drag coefficients occur near the hub and the casing, higher deviations are expected. In view of these facts, extremely careful and accurate measurements are necessary to establish a reliable cascade performance. Accurate calibrations of all instruments, especially of the wedge probe and static pressure probe, have to be established before the internal continuity and reliability of the results can be checked and final calculations performed.

Results of the detailed calibrations are mentioned in the next section where the test procedure is described generally.

IV. TEST PROCEDURE

The strain gage was first calibrated over a wide range of pressures using a water manometer as a reference station as shown in Fig. 5. The calibration was usually checked after each test run and was found fairly good for all the measurements. The flow angles at the inlet and discharge station were measured for different flow rates. The angles at each radial

station were obtained by rotating the probe holder to that position where the differential pressure of both sides of the wedge probe indicated zero on the Baldwin bridge circuit. The test circuit of the tubing was arranged in such a way that all air bubbles could be removed by bleeding the system as shown in Fig. 5. The speed of the pump and the service pump motor was controlled by automatic and manual control. The water level of the test pit was kept constant at the 3.0 ft mark above the laboratory floor. Two angle measurements were obtained for each flow rate, which showed very good agreement. After consistent flow angles were established, the total and static pressures were measured at each station with reference to a total pressure at the middle passage of the inlet or three static pressure taps placed symmetrically around the inlet diameter of the casing. Each probe, i.e., static pressure probe, ducted, and boundary layer total pressure probes, was set according to the respective flow angles and the magnitude of these pressure differentials was read on the Baldwin indicator.

Special care was necessary for reading average values of static pressure differentials because of the unsteady characteristic of the test system and the small pressure gradient across the impeller passage. Several measurements were obtained and repeated very well. The torque was measured by the reaction torque of the motor casing on a strain gage which was connected to an accurate mirror galvanometer. The torque is measured by weights after the zero position is calibrated. The static pressure probe was calibrated in the free surface tunnel of the hydrodynamic laboratory and the test section itself, recording nearly negligible

deviations. It was found that the wedge probe is mainly responsible for errors in the range of 1^{o} to 3^{o}. The wedge probe was calibrated using an airjet and the test section where the blades were removed. The zero position of both calibrations did not coincide because the alignment of the probe differs somewhat in the actual test set-up.

V. DATA REDUCTION AND PRESENTATION OF RESULTS

1. Velocity Profiles.

Two separate sets of downstream velocity profiles were calculated from the measured velocity head and flow angle. In the first case test runs were conducted for the following flow rates, indicated by the venturi meter: φ_i = 0.280, 0.2835, 0.290, 0.300. The accuracy of the measurements is checked by comparison of the mass-averaged flow rate with the flow rate indicated by the venturi meter. The mass averaged flow rate is defined by the following equation;

$$\bar{\varphi} = \frac{\int_{\eta_h}^{\eta_T} \eta \varphi \, d\eta}{\int_{\eta_h}^{\eta_T} \eta \, d\eta} \qquad (1)$$

and is obtained by numerical integration. Since an average error of about 4 percent was found, new measurements were necessary in view of the desired accuracy. A new wedge probe was manufactured and calibrated together with all other probes. Then a new reference station was selected by placing three static pressure taps symmetrically in the plane of the upstream measuring station. It was learned from the first measurements that a boundary-layer blockage of about five percent occurs at the upstream station. Therefore, only the two flow rates are

measured again whose average value represents the design flow rate $\varphi_d = 0.315$. The two flow rates are indicated by the venturi meter to be $\varphi_i = 0.290$ and $\varphi_i = 0.300$.

Figure 6 shows the upstream velocity profile for $\varphi_i = 0.300$ with about five percent higher velocities at the middle passage than indicated by the venturi meter. Two measurements are carried out for $\varphi_i = 0.300$, one without blades and zero speed of the impeller. Little difference is shown by the two respective curves of Fig. 6. The boundary blockage seems to be reduced to a small amount at casing and hub, when the blades are rotating. Generally the highest velocity defect remains the same at the casing in both cases. The same effect is already reported in (11). The velocity distribution is checked by the flow rate $\varphi_i = 0.290$ and a linear relationship is found, which is to be expected. The accuracy of the inlet measurements is in the range of 0.60 percent, obtained by comparison of the mass-averaged and the indicated flow rate. This excellent result is valid for both cases, with and without blades. It can be concluded that the static pressure probe and the wedge probe are performing well and are able to investigate the actual flow pattern.

Figures 7 and 8 show the velocity profiles downstream for the indicated flow rates $\varphi_i = 0.290$ and $\varphi_i = 0.300$. The velocity of the middle passage is higher than the respective inlet velocity. This is apparently due to increased boundary-layer blockage at casing and hub. The velocity increase amounts to about two percent referring to the inlet profile of both flow rates. Both downstream profiles are nearly symmetrical with respect to the middle passage, only the velocity defect

is somewhat higher at the casing. The measured angles of the absolute flow are also shown in these diagrams. The angles are checked several times and repeat fairly well with deviations of about 1/4 degree. The measured mass-flow rate of $\varphi_i = 0.300$ deviates by about one percent and that of $\varphi_i = 0.290$ by about 0.42 percent from the mass flow indicated by the venturi meter.

The static pressure distribution agrees perfectly with theoretical predictions, calculated from the following equation

$$\psi_H = \frac{1}{2}\left[\left(\frac{\varphi^2 \tan^2\gamma_{abs}}{\eta}\right)_{hub} + \left(\frac{\varphi^2 \tan^2\gamma_{abs}}{\eta}\right)\right](\eta - \eta_h) + \frac{h_h}{\left(\frac{u_T^2}{g}\right)} \qquad (2)$$

which is derived from the simple equilibrium condition

$$\frac{1}{\rho}\cdot\frac{dp}{dr} = -\frac{c_u^2}{r} \qquad (3)$$

as shown in Appendix II. Equation (2) is evaluated by taking small intervals from hub to tip. Since the static pressure is measured several times near the hub and is consistent, its value is used as the reference pressure in the above equation. Figures 9 and 10 show the theoretical and measured pressure distributions. Small deviations occur near the boundaries, while the middle passage performs exactly in accordance with the simple, two-dimensional theory.

2. Streamline Shift between Inlet and Discharge Station.

The streamline shift is calculated between the measuring stations upstream and downstream by satisfying the continuity equation graphically.

A dimensionless flow-parameter

$$\Delta q = \frac{\Delta Q}{2\pi \cdot r_T^2 \cdot u_T} = \eta \varphi \cdot d\eta \qquad (4)$$

is plotted versus the radius ratios η_1 and η_2. The difference of the η ordinates indicates immediately the streamline shift for a given capacity. Finally the percentage streamline shift is plotted in Fig. 11 for $\varphi_i = 0.290$ and $\varphi_i = 0.300$. The highest shift of about 1.8 percent occurs near the hub section for the flow rate $\varphi_i = 0.300$. For the other flow rate, $\varphi_i = 0.290$, the largest displacement of about 1.3 percent is again near the hub. The trend of both curves seems to be similar, indicating a positive shift at the hub and very small negative shift at the tip. Nearly two-dimensional flow exists at the middle passage $\eta = 0.80$ to $\eta = 0.95$, where it is expected that the experimental data will be best.

3. Total Pressure Loss of Each Streamline.

The total pressure loss associated with each streamline is derived from the Bernoulli equation of the relative flow.

$$\frac{P_1}{\gamma} + \frac{w_1^2}{2g} - \frac{u_1^2}{2g} = \frac{P_2}{\gamma} + \frac{w_2^2}{2g} - \frac{u_2^2}{2g} + \frac{\Delta P_{tot}}{\gamma} \qquad (5)$$

The total-pressure loss is presented in dimensionless form by the following equation

$$\omega = \frac{\left(\frac{\Delta P_{tot}}{\gamma}\right)}{(u_T^2/g)} = \frac{\Delta h_{st,1-2}}{(u_T^2/g)} + \frac{1}{2}\left[(\varphi_1^2 - \varphi_2^2) + 2\eta_2 \varphi_2 \tan\gamma_{abs} - \varphi_2^2 \tan^2\gamma_{abs}\right] \qquad (6)$$

which uses only measured quantities. Equation (6) is derived in Appendix II. The streamline shift is considered by selecting the actual

values φ_1, φ_2, ζ_2, Δh_{st} for each streamline. Figure 12 illustrates the total pressure loss of both flow rates. The loss coefficient is plotted versus the radius ratio of the downstream station. Both curves have a parabolic shape with minimum loss from $\omega = 0.005$ to $\omega = 0.007$ at the flow passage $\eta = 0.80$ to $\eta = 0.816$. Near the hub and casing the losses are of the same order with about $\omega = 0.04$ to $\omega = 0.06$ for both measurements. The total pressure loss of the smaller flow rate is slightly higher at the middle passage. This is due to higher head generation. The drag coefficients of the design-flow rate are also shown in this diagram, demonstrating again the hgihest losses near the hub. A detailed discussion of lift and drag coefficients follows in the next section.

4. Lift, Drag, and Lift Slope (d_{CL}/d_a) of Each Stream-line.

Lift and drag coefficients of two-dimensional cascades are only defined for velocity triangles of constant meridional components. The meridional velocity is expressed by the dimensionless velocity coefficient φ. In the case being investigated it is found that the axial velocity is not constant along each stream-line. This is due to some average stream-line shift. The amount of the shift is shown in Fig. 11. However, the measurements upstream and downstream of the impeller do not explain the source of the observed shift, which might be caused by the impeller alone, by non-uniform blockage of the boundary-layers on hub and casing downstream of the impeller, or by both effects together. A possible interference of the boundary-layer blockage and the stream-line shift caused by the impeller alone cannot be determined by simple methods. Therefore, it is assumed that the performance may be

approximated by using mean values of the up and downstream meridional velocities and their radial positions. In other words a fictitious or comparative cascade is thought of as being at the average radial position

$$\bar{r} = \frac{r_1 + r_2}{2} \tag{7}$$

with the constant meridional velocity

$$\bar{\varphi} = \frac{\varphi_1 + \varphi_2}{2} \tag{8}$$

The performance of that two-dimensional cascade is defined by the average lift and drag coefficients, which are calculated in the usual manner as shown below. The lift coefficient is obtained from the well known equation: (10)

$$c_L = \frac{2}{\bar{\sigma}} \cos\beta_\infty' \left[\tan\beta_1' - \tan\beta_2' \right] - c_D \cdot \tan\beta_\infty' \tag{9}$$

The above equation is evaluated by calculating first the inlet and discharge angles of the fictitious cascade. To distinguish the measured from the averaged values, primed letters or numbers are assigned to the fictitious cascade plane. The discharge angle β_2' is found from the measured quantities by using the conservation of momentum $(c_u u)_2$:

$$\tan\beta_2' = 1 - \frac{\varphi_2}{\bar{r}} \cdot \tan\gamma_{abs} \tag{10}$$

The inlet angle is defined by:

$$\tan\beta_1' = \frac{\bar{r}}{\bar{\varphi}} \tag{11}$$

Then the mean angle β_∞' is found from the condition of the mean relative velocity:

$$\tan\beta_\infty' = \frac{1}{2}\left(\tan\beta_1' + \tan\beta_2'\right) \tag{12}$$

The drag coefficients are derived from the total pressure-loss coefficients. The latter are related to the cascade plane by the following equation

$$c_3 = \frac{2}{\sigma}\left(\frac{\cos\beta_\infty'}{\bar{\varphi}}\right)^2 \cdot \cos\beta_\infty' \cdot \bar{\omega} \tag{13}$$

which is also derived in Appendix II. Finally, the lift and drag coefficients of the design flow rate $\varphi_d = 0.295$ are presented in Fig. 13 as average values of the measured flow rates $\varphi_1 = 0.290$ and $\varphi_2 = 0.300$. The efficiency e of a cascade can be shown to be (17)

$$e = 1 - \left(\frac{c_D}{c_L}\right)\frac{1}{\sin\beta_\infty' \cdot \cos\beta_\infty'} \tag{14}$$

and is plotted for each radius ratio in Fig. 13 for the design flow rate also. The highest efficiency occurs at the radius ratio = 0.800 with a value of e = 0.94. This efficiency corresponds to a lift coefficient of $C_L = 0.525$ and a drag coefficient $C_D = 0.006$. Theoretical lift coefficients, lift data of Ref. (11) and isolated lift coefficients are compared with the measured, averaged lift coefficients in Fig. 13 also.

Finally, the lift slope $(dC_L/d\alpha)$ is obtained from finite differences of the respective lift coefficients and mean angles of the two measured flow rates according to the equation:

$$\frac{dc_L}{d\alpha} \approx \frac{\Delta c_L}{\Delta\beta_\infty'} \tag{15}$$

The result is plotted versus the radius ratio in Fig. 14, and is compared with theoretical predictions. In Fig. 14 the lift slope is presented in

terms of the cascade coefficient k, defined by Weinig as:

$$K = \left(\frac{dc_L}{d\alpha}\right) \Big/ \left(\frac{dc_L}{d\alpha}\right)_{isolated} \tag{16}$$

Due to the very small angles of attack and small differences in C_L, only approximate, graphically averaged results can be presented, which seem to deviate unexpectedly from theoretical predictions at hub and tip section. Comparison with values of the first set of measurements reveals the same trend for the cascade factor. In that case differences are obtained between the following flow rates: φ = 0.2835, 0.290, 0.300. Therefore it can be concluded that accurate measurements of the lift slope or cascade factor k are beyond the accuracy of the performed calculations and measuring instruments. But the trend of the cascade factor seems to be valid for the mean passage, where three-dimensional effects and total pressure losses are found to be negligible.

5. Torque and Performance Measurements.

The measured torque values are presented by the dimensionless torque coefficient, τ , which relates head and flow coefficients to the efficiency by the following equation:

$$e = \frac{\psi \cdot \varphi}{\tau} \tag{17}$$

The torque of the impeller was measured at the beginning of the test program. The performance curve of the middle passage was established at the same time and compared with the results reported by Ref. (11). Efficiencies, head and torque coefficients of both tests are plotted versus the flow rate in Fig. 15. It is noted that the measured torque coefficients agree exactly with those given in Ref. (11), only the head coefficients are

about ten percent lower. This reduces the efficiency by ten percent. For example, the efficiency for $\varphi = 0.300$ is calculated to be $e = 0.80$ instead of $e = 0.90$. Since the difference of both independent measurements could not be explained, the test facilities were checked carefully to assure the same conditions. It was found that the radial clearance of the impeller was not uniform and amounted to a mean value of 0.027 in. Since such a large clearance was not anticipated, the impeller was repaired and a uniform clearance of 0.005 in. was obtained. New torque and performance measurements were then conducted. Their result is plotted in Fig. 15. Comparison with the previous result shows that the head and torque increased about ten percent, while the efficiency remains the same.

Larger deviations of both head distributions are noticed in the range of smaller flow rates. This is mainly due to different instrumentations and measuring techniques. The old data are obtained with a water manometer, while the new measurements are conducted by employing a high precision strain gage in connection with a Baldwin bridge circuit and amplifier. It is believed that the last method gives more accurate results. For example, the shut-off head could not be measured with the water manometer, but is determined by the strain gage to be $\psi = 0.40$. The performance curve is completed in the range of small flow rates by the last technique and shows nearly a straight line for versus φ . An unstable point is indicated for the flow rate $\varphi = 0.110$, as expected for an axial flow pump of this geometry.

The accuracy of the presented test data is checked finally by comparing the overall performance, which is predicted independently by

torque, total-pressure loss and cascade-loss measurements. The torque measurements indicate an overall efficiency of e = 0.804 for the design flow rate $\varphi_d = 0.315$. The overall efficiency based on mass-averaged total-pressure loss

$$\bar{\omega} = \frac{\int_h^{\bar{r}} \eta \varphi \omega \cdot d\eta}{\int_h^{\bar{r}} \eta \varphi \, d\eta} \tag{18}$$

and mass-averaged total head

$$\bar{\psi} = \frac{\int_h^{\bar{r}} \eta \varphi \psi \, d\eta}{\int_h^{\bar{r}} \eta \varphi \, d\eta} \tag{19}$$

is calculated according to the relation

$$e = \frac{\bar{\psi}}{\bar{\psi} + \bar{\omega}} \tag{20}$$

and amounts to e = 0.82. The mass-averaged cascade efficiency is obtained from the following equation

$$\bar{e}_c = \frac{\int_h^{\bar{r}} \eta \varphi e_c \cdot d\eta}{\int_h^{\bar{r}} \eta \varphi \, d\eta} \tag{21}$$

and can be shown to be in the neighborhood of e = 0.80 to e = 0.83. As a last check on the consistency of the experimental data the torque is calculated from the downstream measured angles and velocities. The torque coefficient is found by numerical integration of the following equation

$$\bar{\tau} = \frac{2}{(1-\eta_h^2)} \int_h^{\bar{r}} \varphi \, k_{cu} \cdot \eta^2 \cdot d\eta \tag{22}$$

which is derived in Appendix II. The calculated value of $\bar{\tau} = 0.041$ deviates only 1.6 percent from the actual torque coefficient. A com-

parison of all efficiencies quoted demonstrates an excellent agreement of all measurements and calculations. In particular the error in C_L and C_D is smaller than ± 2 percent. The head and flow coefficients are measured within 0.50 percent as reported earlier. Therefore, it can be concluded that very consistent and reliable results are obtained. The possibility of predicting these results by various cascade theories is next examined.

VI. THEORETICAL PERFORMANCE CALCULATIONS

The theoretical performance is calculated for the design flow rate with zero angle of attack by following several methods, which account for the effect of the blade thickness on C_L and lift slope. In all cases the two-dimensional, incompressible inviscid and irrotational flow is assumed. The cascade calculations are presented here and are later compared with the experimental results. Deviations between theoretical and experimental results are anticipated in view of the viscous losses. Therefore, an attempt is made to estimate the viscous effect on the cascade performance as shown in the last section of chapter VII.

1. Schlichting's Method of Singularities.

The two-dimensional performance of each cascade section is calculated by the method outlined by Schlichting in (17). Schlichting shows in this paper, that the aerodynamic parameters can be found for any cascade geometry by the method of singularities. This method was first developed by Birnbaum (18) and Glauert (19) for the isolated airfoil. Schilhansl (20), Betz (21) and many others have extended the singularity method to particular cascades of thin airfoils. The general solution for

any blade shape is presented by Schlichting. He also includes the thickness of the profile. It is the basic idea of this method, that any airfoil may be decomposed into a camber line and associated thickness profile. As an approximation, the latter is distributed on the chord rather than on the camber line. The flow field around the cascade can now be described by superposition of the flow field around the thickness profile and the flow with angle of attack around the camber line without thickness. The singularity method replaces the camber by a continuous vortex distribution and the thickness profile by a continuous sink-source distribution. The effect of the cascade can be calculated by superposition of the singularities of all blades. The magnitude of the singularities has to be determined by satisfying the cinematic boundary conditions due to the given camber and thickness profile. Schlichting uses the exact boundary conditions, including all induced velocities. Because the existing thin airfoil theories partly neglect the induced velocities, Schlichting claims a better result. The aerodynamic parameters are given in closed integral form in the case of the isolated airfoil but are necessary to be presented by series expansions for the cascade. This is mainly due to the complex mathematics involved for calculating the induced velocities according to the Biot-Savart law. The coefficients of the series are determined by satisfying the boundary conditions due to thickness and camber. Since Schlichting distributes the singularities on the chord instead of on the camber, the boundary conditions can be satisfied approximately on the chord as done by all thin airfoil theories. Generally the boundary conditions have to be satisfied at infinite many points on the chord.

However, a "three-point method" may be adopted for practical applications (22). The three-point method satisfies the boundary conditions on the 3/12, 7/12, and 11/12 points of the chord. This reduces the infinite number of equations to a system of only six linear equations. Each equation has six unknowns and can be solved by the method of determinates. Scholz (22) and Wieghardt (23) have demonstrated that the three-point method gives nearly exact solutions for isolated airfoils. Schlichting uses the same principle for the cascade and finds close agreement of this method with exact solutions and actual test results as outline in his paper (17). Schlichting's three-point method is applied in this investigation. The aerodynamic parameters are then found by solving the system of six linear equations, each with six unknowns as mentioned above. An accurate, converging solution is determined by three successive approximations as suggested by Schlichting. The solution is somewhat simplified because certain coefficients are presented by Schlichting in tables for various cascade configurations. However, more time was necessary than reported by Schlichting for determination of lift, lift slope and pressure distributions at three radial positions. Instead of 27 hours as he reports for a typical cascade, about two months of continuous work were taken up for completion of the calculations. In view of the time involved it seems desirable to work out general solutions for most common compressor and turbine cascades of NACA 65 camber lines and several thickness distributions. Meller has recently published such solutions for the symmetrical cambered airfoil families (25). The result is presented in several design charts, not available at the time

when this program was started. A comparison between the predicted performance obtained by Schlichting's method with Bowerman's three-dimensional theory and other thin airfoil theories is shown in Fig. 16. In the case of zero thickness, Schlichting's theory shows about 5 percent lower values than Hlawka's two-dimensional theory (25), and deviates about 8 percent from Rannie's approximate solutions as reported in Ref. (11). The result is presented as percent difference from the isolated lift coefficient as given in Ref. (11). From Fig. 16 it can be seen that all cascade theories without thickness deviate about 15 to 20 percent from the three-dimensional prediction of Ref. (11). Schlichting's two-dimensional theory predicts nearly the same lift coefficients as Bowerman's three-dimensional theory. Both curves of lift versus radius ratio are congruent and deviate negligibly at the hub. This result illustrates the general validity of two-dimensional cascade theories including blade thickness.

The cascade factor k is predicted for the case with and without thickness. Figure 14 presents these results for different radius ratios. Schlichting's theory shows negligible deviations in both cases. Rannie's result, however, deviates about two percent from Schlichting's theory. It may be recalled that Rannie's theory does not include blade thickness (9).

Figure 19 illustrates the theoretical pressure distributions in terms of a static pressure differential coefficient c_p. The experimental pressure distributions of Ref. (11) are also shown for comparison. Finally, the results obtained by Schlichting's exact theory are compared with Meller's charts for the NACA 65 airfoil families of 9 percent

thickness. Good agreement is found in the range where his curves could be interpolated for the given cascade.

2. Simple Approximation of Thickness Effect in the Cascade by a Two Point Method.

Schlichting's exact theory is still complicated and consumes too much time for practical applications. Meller's charts, however, do not permit a basic understanding as to how thickness affects the lift of an isolated or staggered airfoil. Therefore, a simple theory is developed which gives a better understanding of the thickness effect in the cascade. This method is outlined below and derived in Appendix III.

To study the effect of thickness the profile is approximated by an ellipse. The major axis is the chord and the minor axis represents the maximum thickness. Schlichting has shown that the profile itself does not induce lift. Therefore its effect on the flow is similar to a uniform flow passing a body without circulation. Since the effect of a circle is known in a uniform flow without circulation, we map the ellipse to a circle in the complex plane. A uniform flow passing the circle without circulation can now be established by the method of complex potentials (26). The flow of the complex plane and the flow of the physical plane are connected by the transformation function. Therefore the thickness effect of the profile can be established in the physical plane.

After some mathematical operations it becomes evident that the effect of thickness is described in our case by a doublet at the one-half point on the chord. The lifting effect of the camber can be described by the effect of a single vortex in the flow with angle of attack. Thin-airfoil theories have shown that accurate results are obtained by placing the

vortex at the one-quarter point of the chord. The boundary conditions have to be satisfied at the three-quarter point as outlined in Ref. (27). A simplified method of singularities can now be applied to the cascade. Instead of continuous vortex and sink-source distributions we use only one vortex at the one-quarter point and one doublet at the one-half point as shown in Fig. 21. The boundary conditions are satisfied at the three-quarter point. After this the lift coefficient is obtained by the method of complex potentials. The result can be expressed in closed form. This is due to the simplicity of the singularities used here. The lift coefficient is given by the following equation derived in Appendix III.

$$C_L = \frac{2}{2\pi\sigma}\left(\sin\alpha + f\,G[\gamma,\sigma]\right)\cdot\frac{1}{F[\gamma,\sigma]} \qquad (23)$$

G and F are functions of solidity and stagger angle alone and are derived in Appendix III. One of the first findings is, that the thickness does not affect the lift slope. However, the lift itself changes proportionally to the thickness. For zero thickness eq. (23) yields the same result as reported by McCormick in Ref. (27). McCormick also shows in his paper that the two point method described, gives good results for flat plates. He concluded that the method may only be applied to cascades of solidity smaller than $\sigma \leq 0.75$.

Equation (23) is evaluated for the middle section, hub, and tip of the present test impeller. The lift coefficient of the middle section agrees exactly with Schlichting's result. The largest deviation is found at the tip section, where the highest stagger angle occurs. In summary it can be concluded that the approximate theory illustrates quite simply the thickness effect in the cascade. The theory is believed to be applicable for all stagger angles smaller than 60° and solidities $\sigma < 0.75$. A com-

parison with other test data should define the applicable range in greater detail.

In view of Schlichting's, Meller's, and the results of the present simple theory, it can be seen that the thickness effect is the most important parameter which causes appreciable deviations of thin-airfoil cascade theories from test results and three-dimensional approximations. In the next chapter we compare the above results with the actual test data.

VII. COMPARISON OF EXPERIMENTAL RESULTS WITH PREDICTIONS OF CASCADE THEORIES

1. Lift Coefficient and Lift Slope.

Figure 13 compares the measured lift coefficients with the theoretical lift coefficients. The latter are obtained from Schlichting's two-dimensional cascade theory as outlined in the foregoing chapter. The theoretical and measured lift coefficients are presented for the design flow rate, $\varphi = 0.295$, with theoretical zero angle of attack. The measured cascade efficiency and the corresponding drag coefficients are included in Fig. 13. In addition, the measured lift coefficients of (14) and the isolated design lift coefficients are compared with our experimental result.

In general, very close agreement is indicated between the two-dimensional cascade theory and the experiment. The experiment demonstrates about four to five percent smaller lift coefficients than predicted at the middle passage, and excellent agreement at the tip and near the hub. At the hub itself higher lift coefficients are measured than calculated. This indicates some angle of attack due to the displacement of the wall boundary-layers. In Fig. 17 the theoretical lift coefficients are corrected

according to measured angles of attack. It is found that small negative angles of attack occur at the middle passage and relative large positive angles of attack at hub and tip due to boundary-layer defect. The corrections are obtained from the theoretical lift slope values of each radial section as given in Fig. 14. The test data are compared with the corrected theoretical lift coefficients in Fig. 17. A surprising close agreement is shown between the theoretical and actual lift coefficients. This holds true over the largest part of the flow passage. Deviations happen mainly at the tip section from $\eta = 0.90$ to $\eta = 1.00$. This may be explained by appreciable boundary layer velocity defects on the casing in connection with some three-dimensional tip clearance flow. Since large losses are indicated at these stations, the two-dimensional cascade theory can hardly predict the correct angle of attack or performance. Besides this the overall prediction of the two-dimensional theory is excellent and far better than the result of (14) as illustrated in Fig. 13. The measured values of (11) indicate about ten percent higher lift coefficients at the middle passage, seven percent higher values at the tip and nearly the same amount as obtained by our measurements. The isolated lift coefficients deviate about 16 percent from the measured values, but follow nearly a similar distribution over the radius as the above wake measurements show.

The theoretical and actual lift slope values are compared in Fig. 14. Lift slope data are obtained from the two measured flow rates $\varphi = 0.290$ and $\varphi = 0.300$ and are presented by the cascade factor k. Nearly the same trend is indicated for slope factors which are reduced

from the first set of measurements with φ = 0.2835, 0.290 and 0.300. Excellent agreement between theoretical prediction and actual values is demonstrated at the middle flow passage from η = 0.80 to η = 0.90. Rather severe deviations, however, are found at hub and tip. This is not surprising, because the total-pressure loss and the streamline shift reach maximum values at those stations. It is also understood that the data at the hub and tip section represent only an approximate result. This is due to the fact that those values could be obtained only from averaged and interpolated test curves. Averaged values are used since the lift slope cannot be reduced accurately enough from the difference, eq. (15), when the difference in α is much smaller than any accuracy of the flow-angle measurement. Therefore it can be concluded that an exact determination of the actual lift slope is beyond the accuracy of our instrumentation and method of data reduction.

In view of the excellent agreement of the predicted and actual lift coefficients, the negligible stream-line shift and the high efficiency of the mean passage flow, it can be argued that the measured slope values may interpret the actual performance most precisely and should be correct. To show this point, the theoretical and actual performance curve of the mean stream section is compared in the next section.

2. Theoretical and Actual Performance of Mean Stream Passage.

The theoretical performance curve ψ versus φ is calculated for the mean stream line by means of the theoretical lift slope and the theoretical lift coefficient at zero angle of attack as shown in Appendix IV. Hereby the flow rates are corrected according to the actual boundary-layer blockage of about ten percent at the inlet station. This effect is

found to be nearly the same for all measured flow rates. In Fig. 18 the theoretical head coefficients are plotted versus the indicated theoretical flow rates, and compared with the actual performance curve. Excellent agreement is found in the range of small angles of attack. Because the theoretical head coefficients do not include viscous losses, corrections are made according to an average drag coefficient of C_D = 0.01. This drag coefficient corresponds closely to the measured coefficient. From inspection of both curves it can now be seen that the corrected head coefficients meet perfectly the actual performance curve for small angles of attack between $\varphi = 0.20$ and $\varphi = 0.35$. Therefore it can be concluded that the measured lift slope of the mean section is correct for the design flow rate, as mentioned in the previous section. This result shows again the validity of the two-dimensional cascade theory. Another check is presented in the next section, where the theoretical and measured pressure distributions of (11) are compared at $\eta = 0.80$.

3. Theoretical and Actual Pressure Distributions.

The measured pressure distributions of the mean blade section are presented for the design flow rate in Fig. 19. These data are taken from Ref. (11). The theoretical prediction of (11) is shown as a dashed curve in this diagram. Since Schlichting's theory is only evaluated by a three point method, only three pressure differentials can be calculated. These three values are plotted in Fig. 19 for comparison. However, the result is sufficient to indicate the trend of the pressure distribution predicted by the two-dimensional cascade theory including blade thickness.

It is noted in Fig. 19 that the two-dimensional prediction seems to agree perfectly with the actual measured value at the leading-edge section. At the middle section and towards the trailing edge somewhat higher values are indicated by our theory, which does not include viscous losses. However, the three-dimensional theory of Ref. (11) predicts lower pressure differentials than measured. The theory of (11) also does not include the viscous losses. This finding demonstrates again the general accuracy and usefulness of the two-dimensional cascade theory. Finally in the next section the possibility of secondary effects of the blade-surface boundary layers on C_L is investigated.

4. Effect of Boundary-Displacement Thickness on the Cascade-Lift Coefficient C_L.

The viscous losses encountered in the flow over the blade profiles of the two-dimensional cascade sections of the impeller are considered in the foregoing analysis by the measured drag coefficients, which reduce the lift coefficients according to eq. (9). However, the lift might also be reduced by alteration of the profile shape due to the displacement effect of the blade-surface boundary layers. This would cause further deviations between experiment and theory and it is therefore desirable to determine the effect of the boundary-layer displacement on C_L of the mean blade section. The mean blade section is chosen for the analysis, since two-dimensional flow and high efficiency found at this section allow the application of simplified boundary-layer concepts for calculating the boundary-layer displacement, as outlined in (2) and (3). In particular, the boundary-layer theory is able to determine the displacement effect by the total displacement thickness of the blade surface boundary layers and their

wake (28), as shown in Fig. 20. This figure is taken from (2). The problem consists therefore of the two steps of calculating first the displacement thickness in the cascade plane from the measurements and investigating secondly the effect of the displacement thickness on the cascade flow.

The first step is done by application of Lieblein's method outlined in (2) and (3) and reported in Appendix IV, which reduces the boundary-displacement thickness of the trailing edge station (as ratio of the chord) to be $(\delta^*/c)_{te} = 0.0148$. This value is then used in the second step to determine approximately the effect of the boundary layer displacement on the cascade flow. For this purpose the cascade of the mean section is approximated by a flat plate cascade of the same solidity and stagger angle. The effect of the displacement thickness on C_L is then investigated for the particular case of zero angle of attack. The displacement thickness itself is distributed linearly on both sides of the chord. In particular it is assumed that the displacement thickness is equal on the upper and lower side as shown in Fig. 22. The cascade flow can now be calculated in the presence of the boundary layer displacement by the method of conformal mapping, as outlined below and in Appendix IV. The well known transformation (9)

$$Z = e^{-i\gamma} \ln\left(\frac{\zeta - \zeta_1}{\zeta + \zeta_1}\right) + e^{i\gamma} \ln\left(\frac{\frac{1}{\zeta} - \bar{\zeta}_1}{\frac{1}{\zeta} + \bar{\zeta}_1}\right) \qquad (24)$$

maps the flat plate cascade to the circle plane. The complex velocity function of this plane can be established by the following relation:

$$F \equiv u - iv = A + iB + \frac{iC}{(\zeta+1)} + \frac{D}{(\pi/2)} \ln\left(\frac{\zeta+1}{\zeta-1}\right) \qquad (25)$$

Since the velocities have to be the same at corresponding points of both planes, the coefficients of the above equation can be determined from the boundary conditions in the cascade plane. The respective points of both planes are correlated by the transformation given in eq. (24). The boundary conditions are discussed in Appendix IV. After the coefficients of eq. (25) are established, we write eq. (25) again for the downstream station. This determines the turning effect of the cascade in the presence of a given, symmetrical, displacement function. In our case it is found that the turning decreases due to the boundary displacement. The turning angle amounts to $\alpha = -0.124^{\circ}$ for the assumed zero angle of attack. This corresponds to a reduction in the lift coefficient, which amounts to $\Delta C_L = -0.0133$. The final result is plotted in Fig. 23 for the cascade of flat plates. Due to lack of more detailed information, it is assumed that the lift slope remains the same in the presence of the boundary layer. This seems to be justified, because the blade thickness also does not influence the lift slope curve. Therefore, the new lift slope curve is shown parallel to the curve without displacement effect. The above result is now applied to the mean section of our impeller. From Fig. 13 it can be seen that the measured and the theoretically predicted lift coefficients deviate about two to three percent. This difference is exactly the amount which is indicated by the above calculations. Therefore it can be concluded that additional effects on C_L are relatively small, but explain the last deviation of theory and experiment. This is the final proof for the validity of the present work.

VIII. SUMMARY AND CONCLUSIONS

To determine the effect of blade thickness, low aspect ratio, high stagger angle, and modest solidity on the performance of an axial flow pump, performance tests and theoretical investigations were conducted using the impeller designed by Bowerman (11). Four independent methods employed to check the internal consistency and accuracy of all measurements revealed that reliable and accurate values of lift and drag coefficients were obtained at each radial blade section. Although the lift slope is found only approximately due to basic limitations of available instruments, the general trend is substantiated by the internal consistency of all measurements. The overall efficiency of the impeller is measured and found to be 82 percent instead of 92 percent as reported in the original investigation by Bowerman. The discrepancy is caused by less accurate instrumentation and measuring techniques of (11) and the small additional mixing losses between the trailing edge and the measuring station downstream used in the present work.

The blade section or cascade performance of each radial position is analyzed in the light of "thin airfoil theories" and modern two-dimensional cascade theories including the effect blade thickness. The viscous loss of each stream-line was determined from total pressure measurements. The lift coefficient was then calculated taking into account the measured stream-line shift and total pressure loss. These calculated values were compared to the predictions of cascade theories with excellent correlation. Deviations of two to three percent on the lift coefficient were observed, however, and they are attributed to the boundary-layer displacement effect on the blade surface. A

simple theory was developed to account for the boundary-layer displacement effect in a cascade of flat plates. The result of this analysis was to cause a change of the lift coefficient of the direction and amount required.

It is concluded that the blade thickness is mainly responsible for the discrepancies between predictions of thin airfoil theories and the actual performance of the axial flow pump observed by Bowerman. Schlichting's two-dimensional cascade theory describes the effect of the blade thickness on the cascade flow very precisely. Not only was the lift coefficient predicted well by this theory but predictions of the lift slope agreed well with the measurements where the latter were available. These results were used to calculate the off-design performance of the mean radial section. The agreement was excellent. The displacement effect of the blade surface boundary-layer is found to be essentially negligible for the Reynolds numbers of these tests. It is also indicated that the displacement thickness does not affect the lift slope curve to any degree. The agreement of Bowerman's theory with the experiments is therefore thought to be largely fortuitous.

In the case of the present machine, the performance of the unit could have been determined with an error of less than ten percent by using isolated airfoil results (at zero angle of attack). The slope of the lift curve should still be determined from the "thin airfoil" cascade theory such as that due to Rannie. As an aid for rapid engineering calculations a simple "two point" method was developed to account for thickness and solidity. It is limited to values of the stagger angle less than about 60° and solidities of about 0.75.

REFERENCES

1. J. E. Garrick: "On the Plane Potential Flow Past a Lattice of Arbitrary Airfoils." NACA Rep. 788, 1944.

2. S. Lieblein, W. H. Roudebush: "Theoretical Loss Relations for Low-Speed Two-Dimensional Cascade Flow." NACA TN 3662, March 1956.

3. S. Lieblein, W. H. Roudebush: "Low-Speed Wake Characteristics of Two-Dimensional Cascade and Isolated Airfoil Sections." NACA TN 3771, October 1956.

4. S. Lieblein: "Analysis of Experimental Low-Speed Loss and Stall Characteristics of Two-Dimensional Compressor Blade Cascades." NACA RM E57A28, March 1957.

5. F. Weinig: "Die Strömung um die Schaufeln von Turbomaschinen." Leipzig, 1935.

6. W. Traupel: "Die Berechnung der Potentialströmung durch Schaufelgitter." Schweitzer Archive f. Angewandte Wiss. und Tech. Bd. 10, Heft 12, 1944.

7. S. Katzoff, Finn, S. Robert and J. C. Laurence: "Interference Method for Obtaining the Potential Flow Past an Arbitrary Cascade of Airfoils." NACA Rep. 879, 1947.

8. G. Klingmann: "Verfahren zur Brechnung der theoretischen Kennlinie von Turbomaschinen." Ing. Arch. XI, 1940 S. 151-

9. J. T. Bowen, R. H. Sabersky, W. D. Rannie: "Theoretical and Experimental Investigations of Axial Flow Compressors." Mechanical Engineering Laboratory, California Institute of Technology, January 1949.

10. NACA Research Memorandum: "Aerodynamic Design of Axial-Flow Compressors." NACA RM E56B03 Volume I, II, III, August 1956.

11. R. D. Bowerman: "Investigation of a Three-Dimensional Design Procedure for Axial-Flow Pump Impellers." ME-Thesis, California Institute of Technology, 1955.

12. A. J. Stepanoff: "Centrifugal and Axial Flow Pumps." Wiley 1948.

13. O'Brien, R.G. Folson: "The Design of Propeller Pumps and Fans." University of California, Publications in Engineering, Vol. 4, 1939.

14. C. Pfleiderer: "Die Kreiselpumpen." Berlin.

15. A. J. Acosta, R. D. Bowerman: "An Experimental Study of Centrifugal Pump Impellers." Hydrodynamic Laboratory, California Institute of Technology, Pasadena, Calif., Report No. E-19.8, August 1955.

16. H. Schlichting: "Problems and Results of Investigations on Cascade Flow." J. Aeron. Sci. VI. 19, 1954.

17. H. Schlichting: "Calculation of the Frictionless, Incompressible Flow for a given Cascade (Direct Problem)." VDI Forschungsheft 447, Ausgabe B, Bd. 21 1955.

18. W. Birnbaum: "Die tragende Fläche als Hilfsmittel zur Berechnung des ebenen Problems der Tragflügel-Theorie." Z. angew. Math.

u. Mech. Bd. 3, 1923.

19. H. Glauert: "Die Grundlagen der Tragflügel und Luftschraubentheorie." Berlin 1929, and "The Elements of Airfoil and Airscrew Theory." Cambridge 1948.

20. M. Schilhansl: "Näherungsweise Berechnung von Auftrieb und Druckverteilung in Flügelgittern." Jb. 1927 Wiss. Ges. Luftf. S. 151/67.

21. A. Betz: "Diagramme zur Berechnung von Flügelreihen." Ing. Arch. Bd. 2, 1931, S. 120.

22. N. Scholz: "Beiträge zur Theorie der tragenden Fläche." Ing. Arch. Bd. 18, 1950.

23. K. Wieghardt: "Über die Auftriebsverteilung des einfachen Rechteckflügels über die Tiefe." Z. angew. Math. Mech. Bd. 19, 1939.

24. G. L. Meller: "An Analysis of Axial Compressor Cascade Aerodynamics." Trans. ASME, Vol.

25. G. E. Hlavka: "An Approximate Theorie for Potential Flow Through Cascades of Airfoils." Ph.D. Thesis, California Institute of Technology, 1954.

26. M. Thomson: "Theoretical Hydrodynamics." Third Edition, 1955, MacMillan, New York.

27. McCormick: "Two Point Method." Jour. Aero. Sci. Readers Forum, October 1956.

28. H. Schlichting: "Boundary Layer Theory." McGraw-Hill 1957.

APPENDIX I

NOTATIONS AND SYMBOLS

C	Absolute velocity
c	Chord length
C_D	Drag coefficient
C_L	Lift coefficient
D	Diameter
e	Efficiency
F	Force
F_D	Drag force
F_L	Lift force
g	Gravity
H	Total head or form factor (δ^*/θ)
h_{st}	Static head
h	Blade height
k	Cascade factor
K_{c_u}	Dimensionless velocity component in tangential direction
N	Speed of impeller
P	Total pressure
Q	Capacity
q	Source strength of unit length
Δq	Capacity factor
r	Radius
s	Spacing
T	Torque

u	Peripheral velocity or induced velocity
U	Velocity along real axia
V	Absolute velocity in complex plane
v	Induced velocity in direction of the imaginary axis
w	Relative velocity
x	Coordinate of real axis
y	Coordinate of imaginary axis or coordinate normal to blade surface
z	Complex coordinates of physical plane
Γ	Circulation
Ω	Total camber angle
α	Angle of attack
β	Flow angle measured between axial direction
γ	Stagger angle
γ_{abs}	Absolute flow angle
δ^x	Boundary layer displacement thickness
ζ	Complex coordinates of circle plane
η	Radius ratio (r / r_T)
θ	Momentum thickness
$\hat{\theta}$	Momentum thickness parameter $(\theta/c)_x \cdot (\sigma/\cos \beta_x)$
θ	Angle of radius vector in circle plane
$\bar{\pi}$	$\pi = 3.1415$
ρ	Density
σ	Solidity c/s
τ	Torque coefficient $T / [\pi \, r_T^3 \, u_T^2 (1 - \eta_h^2)]$

φ Flow coefficient or flow rate (c_m/uT)

ψ Head coefficient $H/(u_T^2/g)$

ω Total pressure loss coefficient $\Delta P_m/\ /(u_T^2/g)$

Subscripts:

D Drag

L Lift

T Tip

h Hub

i Indicated

l Lower surface of blade

m Meridional

tot Total

te Trailing edge

u Tangential or upper surface of blade

∞ Mean values of cascade

0 Free stream values

o Conditions of zero angle of attack

1 Upstream measuring station

2 Downstream measuring station

Other Notations:

$'$ Ideal cascade plane

$\bar{}$ Mean, averaged values

APPENDIX II

DATA REDUCTION

1. Calculation of Mass Averaged Flow Rate.

The data are reduced by using dimensionless parameters. The through flow or meridional velocity component c_m is determined by the dimensionless flow coefficient

$$\varphi = c_m / u_T \tag{1}$$

u_T is the tip speed of the impeller at the radius r_T. Each radial position is described by the dimensionless radius ratio η.

$$\eta = r / r_T \tag{2}$$

The mass averaged flow rate $\bar{\varphi}$ is obtained from the definition

$$\bar{c_m} = \frac{2\pi \int_{r_h}^{r_T} r \cdot c_m \cdot dr}{2\pi \int_{r_h}^{r_T} r \cdot dr} \tag{3}$$

which can be written in dimensionless form by using the above relations and the actual dimensions of the impeller:

$$\bar{\varphi} = \frac{\int_h^{\bar{\eta}} \eta \varphi \, d\eta}{\int_h^{\bar{\eta}} \eta \, d\eta} = 3.121 \int_h^{\bar{\eta}} \varphi \cdot \eta \cdot d\eta \tag{4}$$

The above equation is evaluated by numerical integration. Then the mass averaged flow rate $\bar{\varphi}$ is compared with the flow rate φ_i indicated by the venturi meter.

2. Theoretical Prediction of the Static Pressure Distribution at the Measuring Station.

The static pressure or static head distribution h(r) is derived from the simple radial equilibrium equation of two-dimensional flow:

$$\frac{dh}{dr} = - \frac{c_u^2}{g \cdot r} \qquad (5)$$

Using a small interval Δr, (c_u^2/r) can be assumed to be linear with respect to r. Then the above equation can be integrated if all values are known at one position. This position is taken at the hub at the radius r_h and the static head h_h. The integrated equation is

$$h = \frac{1}{2g} \left[\left(\frac{c_u^2}{r}\right)_h + \left(\frac{c_u^2}{r}\right) \right] (r - r_h) + h_h \qquad (6)$$

which may be rewritten by using the dimensionless parameters , and the relation

$$c_u = c_m \cdot \tan \gamma_{abs}$$

to present finally the theoretical prediction of h(r) at the measuring station:

$$\psi_{st} = \frac{h}{(u_T^2/g)} = \frac{1}{2} \left[\left(\frac{\varphi^2 \cdot \tan^2 \gamma_{abs}}{\eta}\right)_h + \left(\frac{\varphi^2 \cdot \tan^2 \gamma_{abs}}{\eta}\right) \right] (\eta - \eta_h) + \psi_{sth} \qquad (7)$$

The angle γ_{abs} is the absolute flow angle as shown in Fig. 1.

3. Total Pressure Loss of Each Streamline.

The total pressure loss is presented by the dimensionless coefficient ω which is defined:

$$\omega = \frac{\left(\frac{\Delta p_{tot}}{\gamma}\right)}{(u_T^2/g)} = \frac{\Delta H}{(u_T^2/g)} \qquad (8)$$

The total pressure loss coefficient is obtained from the Bernoulli equation of the relative flow:

$$h_1 + \frac{w_1^2}{2g} - \frac{u_1^2}{2g} = h_2 + \frac{w_2^2}{2g} - \frac{u_2^2}{2g} + \frac{\Delta p_{tot}}{\gamma} \tag{9}$$

Inspection of the velocity triangles gives the relations

$$w_1^2 - u_1^2 = c_{m_1}^2 \tag{10}$$

$$w_2^2 - u_2^2 = c_{u_2}^2 + c_{m_2}^2 - 2 u_2 c_{u_2} \tag{11}$$

which define the total pressure loss coefficient by inserting them in the above equation and using dimensionless parameters as follows:

$$\omega = \frac{\Delta h_{1-2}}{(u_T^2/g)} + \frac{1}{2}\left[(\varphi_1^2 - \varphi_2^2) + 2\eta_2\varphi_2 \tan\gamma_{abs} - \varphi_2^2 \cdot \tan^2\gamma_{abs}\right] \tag{12}$$

4. Calculation of Drag Coefficient C_D from Total Pressure Loss Coefficient ω.

The drag force is given for uniform outlet conditions according to Fig. 1:

$$F_D = F_n \cdot \sin\beta_\infty - F_m \cdot \sin\beta_\infty \tag{13}$$

Since two-dimensional flow is assumed, the axial force F_m results only from the change in static pressure across the blades. The pressure change is known from the Bernoulli equation of the relative flow. This defines the axial force F_m

$$F_m = s(p_2 - p_1) = s\left[\frac{1}{2}\rho(w_1^2 - w_2^2) - \Delta p_{tot}\right] \tag{14}$$

The force in the tangential direction F_u is determined by the momentum equation:

$$F_u = s \rho c_m (w_{u_1} - w_{u_2}) \tag{15}$$

Equation (13) becomes, with equations (14) and (15):

$$\frac{F_D}{s \cos\beta_\infty} = \rho c_m (w_{u_1} - w_{u_2}) \tan\beta_\infty - [\tfrac{1}{2} \rho (w_1^2 - w_2^2) - \Delta p_{tot}] \tag{16}$$

With substitution of the following relations of the velocity triangles

$$\tan\beta_\infty = \frac{w_{u_1} + w_{u_2}}{2 \cdot c_m} \tag{17}$$

$$w_1^2 - w_2^2 = w_{u_1}^2 - w_{u_2}^2 \tag{18}$$

into eq. (16) the drag force F_D is obtained as follows:

$$F_D = s \cos\beta_\infty - \Delta p_{tot} \tag{19}$$

The drag coefficient is defined by:

$$c_D = \frac{F_D}{\tfrac{1}{2} \rho c \cdot w_\infty^2} \tag{20}$$

Then we finally obtain from

$$w_\infty = w_1 \frac{\cos\beta_1}{\cos\beta_\infty} \tag{21}$$

and

$$w_1 = \frac{\varphi_1}{\cos\beta_1} u_T \tag{22}$$

the relation between C_D and the total pressure loss coefficient:

$$C_D = 2 \cdot \left(\frac{s}{c}\right) \left(\frac{\cos\beta_\infty}{\varphi_1}\right)^2 \cdot \cos\beta_\infty \cdot w \tag{23}$$

5. Calculation of Torque Coefficient τ from Downstream Measurements.

The torque input to each streamline is found by using the torque definition:

$$\Delta T = \rho \cdot r \cdot c_u \cdot dQ \tag{24}$$

With

$$dQ = 2\pi \cdot r \cdot c_m \cdot dr \tag{25}$$

and using the dimensionless flow coefficient φ, the radius ratio η, and the (tangential) velocity coefficient k_{cu}

$$k_{cu} = c_u / u_T \tag{26}$$

equation (24) can be integrated from hub to tip.

$$\bar{T} = 2\pi \cdot r_T^3 \cdot u_T^2 \int_h^{\bar{r}} \varphi \, k_{cu} \cdot \eta^2 \cdot d\eta \tag{27}$$

The torque is now presented by the dimensionless torque coefficient according to the definition:

$$\tau = \frac{\bar{T}}{\pi \rho \, r_T^2 u_T^2 \left(1 - \eta_h^2\right)} \tag{28}$$

By inserting eq. (28) in (27) the final torque equation is found in dimensionless form and applied to the geometry of our impeller.

$$\tau = 3.12 \int_h^{\bar{r}} \varphi \cdot k_{cu} \cdot \eta^2 \cdot d\eta \tag{29}$$

6. Theoretical Performance Prediction of Mean Streamline at $\eta = 0.80$.

The theoretical performance curve ψ versus φ is obtained at $\eta = 0.80$ by selecting several values of angle of attack and then calculating the respective lift coefficients from the known relation:

$$c_L = \alpha_\infty \cdot \left(\frac{dc_L}{d\alpha}\right) + c_{L_0} \tag{30}$$

The lift slope and the theoretical lift coefficient C_{Lo} of zero angle of attack are calculated from the two-dimensional cascade theory including thickness as outlined before (see Fig. 13 and Fig. 14). The head coefficient

$$\psi = \frac{H}{(u_T^2/g)} = \eta \cdot \frac{c_u}{u_T} \tag{31}$$

is determined from the well known relation

$$\psi_{id} = \frac{1}{2}\left(\frac{c}{s}\right) \cdot \eta \; \frac{c_L \cdot \varphi}{\cos\beta_\infty} \tag{32}$$

where φ is found for given angle of attack from

$$\varphi = \frac{\eta}{\tan\beta_1} \tag{33}$$

and

$$\tan\beta_1 = \frac{c_L}{4\left(\frac{c}{s}\right) \cdot \cos\beta_\infty} + \tan\beta_\infty \tag{34}$$

α_∞ and β_∞ are related according to Fig. 1 as follows:

$$\beta_\infty = \alpha_\infty + \gamma \tag{35}$$

The above equation for ψ_{id} does not consider losses. In the case of total

pressure losses eq. (32) is corrected by the total efficiency according to the definition:

$$e_{tot} = \frac{\psi_{id} - w}{\psi_{id}} = \frac{\psi}{\psi_{id}} \tag{36}$$

The efficiency is established by inserting eq. (32) and eq. (23) of section 4 of this appendix in the efficiency relation. This gives the following equation:

$$e_{tot} = 1 - \left(\frac{c_D}{c_L}\right) \frac{\varphi}{\eta \cdot \cos^2\beta_\infty} \tag{37}$$

After that, the actual head coefficient is calculated according to eq. (36) when viscous losses are to be considered.

$$\psi = \frac{1}{2}\left(\frac{c}{s}\right) \cdot \eta \cdot \frac{c_L \cdot \varphi}{\cos\beta_\infty} \left[1 - \left(\frac{c_D}{c_L}\right) \frac{\varphi}{\eta \cos^2\beta_\infty}\right] \tag{38}$$

The final result is presented in Fig. 18 .

APPENDIX III

A SIMPLE APPROXIMATION TO THE LIFT IN A TWO-DIMENSIONAL CASCADE OF THICK AIRFOILS

1. Method.

Replace effect of airfoil due to lift by vortex at the 1/4 chord point. Approximate effect of thickness by appropriate doublet at the 1/2 chord point. Then satisfy boundary conditions at the 3/4 chord point.

2. Equivalent Doublet to Replace Thickness.

The ellipse of length c and maximum thickness d is mapped into a circle of radius a in the t plane by

$$\zeta = \frac{c}{2(a+1)}\left(t + \frac{a}{t}\right) \tag{1}$$

The ratio of maximum thickness to chord is

$$\left(\frac{d}{c}\right) = f = \frac{a-1}{a+1} \quad \text{or} \quad a = \frac{1+f}{1-f}$$

In the t plane the potential for a uniform flow past the ellipse without circulation is

$$F \equiv \varphi + i\psi = \frac{\pi c(1-f)}{4}\left[e^{-i\alpha}t + \frac{a^2 e^{i\alpha}}{t}\right] \tag{2}$$

where α is angle of attack to the ellipse. Inverting equation (1):

$$t = \frac{1}{1-f}\left\{\frac{2\zeta}{c} + \sqrt{\frac{4\zeta^2}{c^2} - (1-f^2)}\right\}$$

Hence the potential becomes in the z plane:

$$F = \frac{\gamma(1-f)c}{4}\left\{ e^{-i\alpha}\frac{2\zeta}{c}\frac{1}{(1-f)}\left[1+\sqrt{1-\frac{1-f^2}{4\zeta^2/c^2}}\right] + \right.$$

$$\left. + \frac{e^{i\alpha}(1+f)^2}{(1-f^2)(1-f)}\cdot\frac{2\zeta}{c}\left[1-\sqrt{1-\frac{1-f^2}{4\zeta^2/c^2}}\right]\right\} \tag{3}$$

We now gather up terms, expand the radical for the case $\zeta/c \gg 1$ and neglect f^2 compared to f to get:

$$F = U\cdot e^{-i\alpha}\zeta + \frac{uc^2}{16}\left[2i\sin\alpha + 2fe^{i\alpha}\right]\cdot\frac{1}{\zeta} \tag{4}$$

Hence the sole effect of thickness is to add a doublet

$$\frac{uc^2}{16}\cdot\frac{2f}{\zeta}\cdot e^{i\alpha}$$

to the flow. We will neglect the small product $\alpha \cdot f$ and write the doublet potential that accounts for thickness as:

$$F_d = \frac{uc^2}{8\zeta}\cdot f \tag{5}$$

3. Solution in Cascade.

Consider a cascade of stagger angle with spacing and the array of singularities as shown in Fig. 21. The vortices are located along the line

$$\zeta = e^{i\left(\frac{\pi}{2}-\gamma\right)}$$

and the doublets along the ray

$$\zeta = c/4 + e^{i\left(\frac{\pi}{2}-\gamma\right)}$$

The potential is

$$F = \frac{i\Gamma}{2\pi} \cdot \sum_{n=-\infty}^{+\infty} \ln\left(z - 2\pi n \cdot e^{i\left(\frac{\pi}{2}-\gamma\right)}\right) + \frac{uc^2 f}{8} \cdot \sum_{n=-\infty}^{+\infty} \left(\frac{1}{z - c/4 - 2\pi n \cdot e^{i(\pi/2-\gamma)}}\right) \quad (6)$$

These series have well known sums:

$$F = \frac{i\Gamma}{2\pi} \ln\left[2\sinh\left(\frac{z \cdot e^{i\gamma}}{2}\right)\right] + \frac{uc^2 f}{16} \cdot e^{i\gamma} \coth\left[e^{i\gamma}\left(\frac{z - c/4}{2}\right)\right] \quad (7)$$

Hence u-iv = dF/dz is

$$u - iv = \frac{i\Gamma}{4\pi} e^{i\gamma} \coth\left(\frac{z \cdot e^{i\gamma}}{2}\right) - \frac{uc^2 f \cdot e^{2i\gamma}}{32} \cdot \frac{1}{\sinh^2\left[\frac{1}{2} e^{i\gamma}(z - c/4)\right]} \quad (8)$$

We are interested in the vertical component of velocity and this is:

$$-v = \frac{\Gamma}{4\pi} \frac{\cos\gamma \sinh(c/2 \cos\gamma) + \sin\gamma \sin(c/2 \sin\gamma)}{\cosh(c/2 \cos\gamma) - \cos(c/2 \sin\gamma)} -$$

$$- \left(\frac{uc^2 f}{32}\right) \frac{\sin 2\gamma \left[\sinh^2(c/8 \cos\gamma)\cos^2(c/8 \sin\gamma) - \cosh^2(c/8 \cos\gamma)\sin^2(c/8 \sin\gamma)\right]}{\left[\sinh^2(c/8 \cos\gamma)\cos^2(c/8 \sin\gamma) + \cosh^2(c/8 \cos\gamma)\sin^2(c/8 \sin\gamma)\right]^2} - \quad (9)$$

$$- \frac{\frac{1}{2}\cos 2\gamma \sinh(c/4 \cos\gamma)\sin(c/4 \sin\gamma)}{\left[\sinh^2(c/8 \cos\gamma)\cos^2(c/8 \sin\gamma) + \cosh^2(c/8 \cos\gamma)\sin^2(c/8 \sin\gamma)\right]^2}$$

To eq. (8) we must add the component parallel to the cascade axis $V_\infty \cdot \sin(\gamma + a_\infty)$ to make the upstream flow have the velocity $V_1 e^{-ia_1}$. The boundary conditions on the foil are then that v = 0 or that the (-v) of eq. (9) be equal to $V_\infty \cdot \sin a_\infty$. We then solve for Γ to get the result:

$$\Gamma = \frac{V_\infty}{F(\gamma,\sigma)} \left(\sin\alpha_\infty + f\, G(\gamma,\sigma) \right) \tag{10}$$

where

$$F(\gamma,\sigma) = \left(\frac{1}{4\pi}\right) \cdot \frac{\cos\gamma \sinh(\pi\sigma\cos\gamma) - \sin\gamma \sin(\pi\sigma\sin\gamma)}{\cosh(\pi\sigma\cos\gamma) - \cos(\pi\sigma\sin\gamma)} \tag{11a}$$

$$G(\gamma,\sigma) = \left(\frac{\pi^2\sigma^2}{8}\right) \left\{ \frac{\sin 2\gamma \left[\sinh^2\left(\frac{\pi\sigma}{4}\cos\gamma\right) \cos^2\left(\frac{\pi\sigma}{4}\sin\gamma\right) \right]}{\left[\sinh^2\left(\frac{\pi\sigma}{4}\cos\gamma\right) \cos^2\left(\frac{\pi\sigma}{4}\sin\gamma\right) + \cosh^2\left(\frac{\pi\sigma}{4}\cos\gamma\right) \sin^2\left(\frac{\pi\sigma}{4}\sin\gamma\right) \right]^2} - \right.$$

$$\left. - \frac{\sin 2\gamma \left[\cosh^2\left(\frac{\pi\sigma}{4}\cos\gamma\right) \sin^2\left(\frac{\pi\sigma}{4}\sin\gamma\right) \right] + \frac{1}{2}\cos 2\gamma \sinh\left(\frac{\pi\sigma}{2}\cos\gamma\right) \sin\left(\frac{\pi\sigma}{2}\sin\gamma\right)}{\left[\sinh^2\left(\frac{\pi\sigma}{4}\cos\gamma\right) \cos^2\gamma\left(\frac{\pi\sigma}{4}\sin\gamma\right) + \cosh^2\left(\frac{\pi\sigma}{4}\cos\gamma\right) \sin^2\left(\frac{\pi\sigma}{4}\sin\gamma\right) \right]^2} \right\} \tag{11b}$$

Now with the result

$$C_L = \frac{2\Gamma}{c \cdot V_\infty} = \frac{2}{2\pi\sigma} \left[\sin\alpha_\infty + f \cdot G(\gamma,\sigma) \right] \cdot \frac{1}{F(\gamma,\sigma)} \tag{12}$$

we have one of the first findings: namely, that thickness does not affect the lift slope curve and that its effect is proportional to the thickness. When f = 0, we get in simpler form and different notation McCormick's result in Ref. (26). There he shows that the two point method gives satisfactory results for lift for $\sigma < 0.75$.

4. Camber.

We take the angle of attack for zero lift to be $-\Omega/4$ where Ω is the total camber. The effective stagger angle is now $\gamma - \Omega/4$, where the γ refers to the stagger angle measured from the chord line. Retaining the notation α_∞ to represent angle to the chord line, the lift coefficient becomes

$$C_L = \frac{\frac{4}{\sigma}\left\{\alpha_\infty + (\Omega/4) + fG(\gamma,\sigma)\right\}\left[\cosh\left(\bar{\pi}\sigma\cos\left(\gamma-\frac{\Omega}{4}\right)\right) - \cos\left(\bar{\pi}\sigma\sin\left(\gamma-\frac{\Omega}{4}\right)\right)\right]}{\cos\left(\gamma-\frac{\Omega}{4}\right)\sinh\left[\bar{\pi}\sigma\cos\left(\gamma-\frac{\Omega}{4}\right)\right] + \sin\left(\gamma-\frac{\Omega}{4}\right)\sin\left[\bar{\pi}\sigma\sin\left(\gamma-\frac{\Omega}{4}\right)\right]} \quad (13)$$

where G is defined by eq. (11b) with γ to be replaced by $\gamma - \Omega/4$ in the case of camber.

APPENDIX IV

EFFECT OF BOUNDARY LAYER DISPLACEMENT THICKNESS ON THE CASCADE FLOW

1. Calculation of Displacement Thickness and Momentum Thickness at Downstream Station.

The total displacement due to the boundary layer thickness δ is defined by the displacement thickness (Ref. (26)

$$\delta^{x}_{tot} = \int_{\delta_e}^{\delta_u} \left(1 - \frac{V}{V_o}\right) dy \tag{1}$$

The momentum loss is given by the momentum thickness

$$\theta_{tot} = \int_{\delta_e}^{\delta_u} \left(1 - \frac{V}{V_o}\right)\left(\frac{V}{V_o}\right) \cdot dy \tag{2}$$

V_o is the free stream velocity and V the velocity in the boundary layer profile. The form of the wake or total boundary layer of upper and lower blade surface is also characterized by the form factor H.

$$H = \delta^{x}/\theta \tag{3}$$

When a power velocity profile is assumed for approximation of the boundary layer profile, the displacement and momentum thickness can be calculated at the measuring station according to Ref. (2). The momentum thickness as ratio of the chord length c is determined by using equation (B18) of Ref. (4).

$$\left(\frac{\theta}{c}\right)_2 = \frac{C_D \cdot \left(\frac{\cos\beta_2'}{\cos\beta_\infty'}\right)^3}{1 + b + \sqrt{1 + b(H_2+2)}} \tag{4}$$

where C_D is the measured drag coefficient and b is given by

$$b = C_D \cdot \left(\frac{\cos\beta_2'}{\cos\beta_\infty'}\right)^3 \left(\frac{\sigma H_2}{\cos\beta_2}\right) \tag{5}$$

The form factor can be estimated from Ref. (3) and is about H = 1.1 for our case. The displacement thickness is now determined by eq. (4).

2. Calculation of Displacement Thickness of Trailing Edge from Downstream Measurements.

The form factor of the trailing edge is obtained by the empirical equation of Ref. (3), which relates the downstream values to the trailing edge as follows.

$$H_k = \frac{1}{1 - \left(1 - \frac{1}{H_2}\right)\left(\frac{(x/c) + 0.025}{0.025}\right)^{1/2}} \tag{6}$$

By using the definition

$$\hat{\theta}_k = \left(\frac{\theta}{c}\right)_k \left(\frac{\sigma}{\cos\beta_k}\right)$$

the momentum thickness parameter can be calculated according to Ref. (3) by an iteration method for solving the equation

$$2\left[1 - \hat{\theta}_k(1+H_k)\right]^2\left\{\left[1 - \hat{\theta}_k(1+H_k)\right] - K_1\left(1 - \hat{\theta}_k H_k\right)^2\right\} =$$

$$K_2\left(1 - \hat{\theta}_k H_k\right)^4 + \left[1 - \hat{\theta}_k(1+H_k)\right]^2 \tag{7}$$

The constants K_1 and K_2 are determined by the parameters of the downstream station: H_2, θ_2, β_2'.

$$K_1 = \frac{1 - \hat{\theta}_2 (1 + H_2) - \frac{1}{2\cos^2\beta_2'}}{\left(1 - \hat{\theta}_2 H_2\right)^2} \tag{8}$$

$$K_2 = \left(\frac{\sin\beta_2' \left[1 - \hat{\theta}_2 (1 + H_2)\right]}{\cos\beta_2' \left[1 - \hat{\theta}_2 H_2\right]^2} \right)^2 \tag{9}$$

After θ_{te} is calculated the flow angle β_{te} is found from the relation

$$\tan\beta_k' = \tan\beta_2' \left[\left(\frac{1 - \hat{\theta}_{te} \cdot H_k}{1 - \hat{\theta}_2 H_2} \right)^2 \left(\frac{1 - \hat{\theta}_2 (1 + H_2)}{1 - \hat{\theta}_k (1 + H_k)} \right) \right] \tag{10}$$

which is taken from (3). The trailing-edge parameters $(\theta/c)_2$, $(\delta^*/c)_2$ are now given according to the previously mentioned definitions:

$$\left(\frac{\theta}{c}\right)_{te} = \hat{\theta}_{te} \left(\frac{\cos\beta_{te}'}{\sigma} \right) \tag{11}$$

$$\left(\frac{\delta^*}{c}\right)_{te} = H_{te} \cdot \left(\frac{\theta}{c}\right)_{te} \tag{12}$$

3. Effect of Boundary Displacement Thickness on the Cascade Flow.

The effect of the total boundary-displacement thickness on the cascade flow is investigated for the case of the flat-plate cascade as

shown in Fig. 22. The cascade is described by the solidity $(c/2\pi)$ and the stagger angle γ. For our special case of zero angle of attack it is assumed that the displacement thickness of the boundary layer is distributed symmetrically and linearly on the upper and lower blade side. Hence the displacement thickness is zero at the leading edge and half the total value of $(\delta^*/c)_{te}$ on each blade surface at the trailing edge. In this case the following boundary conditions are valid in the cascade plane:

Velocities induced due to an angle of attack α do not exist:

$$v_\alpha = \frac{\delta_u^* - \delta_e^*}{2c} V_\infty = 0 \tag{13}$$

The only induced velocities are due to the displacement thickness, and are given by the relation:

$$v_{th} = \pm \frac{\delta_u^* + \delta_e^*}{2c} \cdot V_\infty = \pm \left(\frac{\delta_{tot}^*}{2c}\right) \cdot V_\infty \tag{14}$$

V_∞ is the mean velocity of the up and downstream components. The up and downstream velocities determine the boundary conditions at $z = -\infty$

$$u - iv = V_1 \cdot e^{-i\alpha_1} = U \tag{15}$$

and $z = +\infty$

$$u - iv = V_2 \cdot e^{-i\alpha_2} \tag{16}$$

The problem is now to find the down-stream values α_2, V_2 for given

up-stream conditions of the cascade. For this purpose the cascade plane is mapped to the circle plane by the well known mapping function (9):

$$z = e^{-i\gamma} \ln\left(\frac{\zeta - \zeta_1}{\zeta + \zeta_1}\right) + e^{i\gamma} \ln\left(\frac{\left(\frac{1}{\zeta}\right) - \bar{\zeta}_1}{\left(\frac{1}{\zeta}\right) + \bar{\zeta}_1}\right) \tag{17}$$

This transformation maps the leading edge to the -1 point and the trailing edge to the +1 point on the circle as shown in Fig. 25. The point $z = -\infty$ corresponds to the point ζ_1 and the point $z = +\infty$ to $-\zeta_1$ in the ζ plane. The absolute value of ζ_1 is found from the given cascade parameters (c/s) and γ according to Ref. (9). This value is determined by the value of ψ as seen from the relation:

$$\zeta_1 = e^{\psi} \cdot e^{i\theta} \tag{18}$$

The exponent ψ is given by evaluating the following equation derived by Ref. (9):

$$\frac{\pi}{2}\left(\frac{c}{s}\right) = \cos\gamma \ln\left(\frac{\sqrt{\cosh 2\psi + \cos 2\gamma} + \sqrt{2}\cos\gamma}{\sqrt{\cosh 2\psi + \cos 2\gamma} - \sqrt{2}\cos\gamma}\right) +$$

$$+ 2\sin\gamma \tan^{-1}\left(\frac{\sqrt{2}\sin\gamma}{\sqrt{\cosh 2\psi + \cos 2\gamma}}\right) \tag{19}$$

The angle θ of eq. (6) is the angle of the vector with the real axis as shown in Fig. 25 and is obtained for given values of $\gamma_1 \psi$ from the relation:

$$\Theta = \bar{\pi} - \tan^{-1}(\tan\gamma \tanh\psi) \tag{20}$$

The flow of the ζ plane is now calculated by using the complex velocity function F = u-iv which is the same at corresponding points of both planes. The flow in the cascade plane is similar to a uniform flow in the presence of a constant source distribution along the chord and a single vortex at the leading edge. The single vortex describes the effect of angle of attack and the source distribution in connection with the uniform flow field the effect of the boundary-displacement thickness. The source strength per unit length is given on each side of the chord according to

$$q = \left(\frac{\delta_k^*}{2c}\right) \cdot V_\infty \tag{21}$$

The complex velocity function is therefore

$$F \equiv u - iv = A + iB + \frac{iC}{\zeta+1} + \frac{D}{(\bar{\pi}/2)} \ln\left(\frac{\zeta+1}{\zeta-1}\right) \tag{22}$$

The constant D is equal to the source strength per unit length. The constants A, B, and C are evaluated by satisfying the boundary conditions in the flow field far up-stream. Equation (22) gives the relation for z = $-\infty$

$$V_1 \cdot e^{-i\alpha_1} = U = A + iB + \frac{iC}{\zeta_1+1} + \frac{D}{(\bar{\pi}/2)} \ln\left(\frac{\zeta_1+1}{\zeta_1-1}\right) \tag{23}$$

A relation between B and C is found from the case of zero displacement

thickness, where the part due to angle of attack is given by the complex velocity -iv

$$-iv = +iB + \frac{iC}{\zeta_1 + 1} \tag{24}$$

Noting for a stream line on the circle

$$\zeta = e^{i\theta}$$

we obtain:

$$-iv = +iB + i\frac{c}{2}\left(1 - i\tan\left(\frac{\theta}{2}\right)\right) \tag{25}$$

By use of the boundary condition (1) eq. (25) reduces to

$$v_\alpha = 0 = B + \frac{c}{2}$$

Therefore

$$B = -c/2 \tag{26}$$

The constants A and C are now obtained from eq. (23) for the case of $\alpha = 0$ and $V_1 = U$

$$\left(\frac{U}{V_\infty}\right) = \left(\frac{A}{V_\infty}\right) + i\left(\frac{C}{V_\infty}\right)\left[\frac{1}{\zeta_1 + 1} - \frac{1}{2}\right] + \frac{1}{\pi}\left(\frac{\delta^*_{tot}}{c}\right)\ln\left(\frac{\zeta_1 + 1}{\zeta_1 - 1}\right) \tag{27}$$

by separating real

$$\left(\frac{U}{V_\infty}\right) = \left(\frac{A}{V_\infty}\right) + i\left(\frac{C}{V_\infty}\right)\mathrm{Im}\left[\frac{1}{\zeta_1 + 1} - \frac{1}{2}\right] + \frac{1}{\pi}\left(\frac{\delta^*_{tot}}{C}\right)\mathrm{Real}\ln\left(\frac{\zeta_1 + 1}{\zeta_1 - 1}\right) \tag{28}$$

and imaginary part

$$0 = i\left(\frac{C}{V_\infty}\right)\mathrm{Real}\left[\frac{1}{\zeta_1 + 1} - \frac{1}{2}\right] + \frac{1}{\pi}\left(\frac{\delta^*_{tot}}{C}\right)\mathrm{Im}\ln\left(\frac{\zeta_1 + 1}{\zeta_1 - 1}\right) \tag{29}$$

The constant C then is found immediately from eq. (29).

$$\left(\frac{c}{V_\infty}\right) = -\frac{\frac{1}{\pi}\left(\frac{\delta_{TA}^*}{c}\right) \mathrm{Im}\ \ln\left(\frac{\zeta_1+1}{\zeta_1-1}\right)}{\mathrm{Real}\left[\frac{1}{\zeta_1+1} - \frac{1}{2}\right]} \tag{30}$$

The imaginary and real part of the above relation is calculated by inspection of Fig. 22 where the vector $(\overrightarrow{\zeta_1 + 1})$ includes the angle θ_2 and the vector $(\overrightarrow{\zeta_1 - 1})$ the angle θ_1, with the real axis. Hence the imaginary part is given

$$\mathrm{Im}\ \ln\left(\frac{\zeta_1+1}{\zeta_1-1}\right) = \theta_2 - \theta_1 \tag{31}$$

where

$$\theta_2 = \cos^{-1}\left(\frac{1 - e^{\psi}\cos\theta}{\sqrt{1 + e^{2\psi} - 2e^{\psi}\cos\theta}}\right) \tag{32}$$

and

$$\theta_1 = \pi - \cos^{-1}\left(\frac{1 + e^{\psi}\cos\theta}{\sqrt{1 + e^{2\psi} + 2e^{\psi}\cos\theta}}\right) \tag{33}$$

The angle θ is determined by equation (20). The real part is found to be

$$\mathrm{Real}\left(\frac{1}{\zeta_1+1}\right) = \frac{1}{\sqrt{1 + e^{2\psi} - 2e^{\psi}\cos\theta}} \tag{34}$$

With C known A is calculated according to equation (28). Now all constants are determined and the problem is solved by satisfying the boundary conditions down-stream. This leads to the relation between

up-stream and down-stream conditions:

$$V_2 \cdot e^{-i\alpha_2} = A + iB + \frac{iC}{(1-\zeta_1)} + \frac{D}{(\pi/2)} \ln\left(\frac{1-\zeta_1}{-1-\zeta_1}\right) \tag{35}$$

The unknowns α_2 and V_2 are obtained by separating again real and imaginary part and determining the absolute values and angles of the vectors $\overrightarrow{(-\zeta_1 + 1)}$ and $\overrightarrow{(-\zeta_1 - 1)}$. In particular, the angle α_2 is found from the relation

$$\alpha_2 = \tan^{-1} \left| \frac{iB + i\,\mathrm{Real}\left(\frac{C}{-\zeta_1+1}\right) + \frac{D}{(\pi/2)}\,\mathrm{Im}\,\ln\left(\frac{-\zeta_1+1}{-\zeta_1-1}\right)}{A + i\,\mathrm{Im}\left(\frac{C}{-\zeta_1+1}\right) + \frac{D}{(\pi/2)}\,\mathrm{Real}\,\ln\left(\frac{-\zeta_1+1}{-\zeta_1-1}\right)} \right| \tag{36}$$

which enables us to calculate V_2 from the real or imaginary part of equation (35). The imaginary and real part of equation (36) is calculated in a similar manner as shown before for the vectors $\overrightarrow{(\zeta_1 + 1)}$ and $\overrightarrow{(\zeta_1 - 1)}$.

To determine the effect of $(\delta^*_{ca}/C)_{te}$ on the lift coefficient C_L the values V_2 and α_2 are referred to the cascade plane by use of the continuity equation

$$\left(\frac{V_2}{V_\infty}\right)' \cos(\gamma + \alpha_2') = \left(\frac{V_1}{V_\infty}\right) \cos\gamma \tag{37}$$

and by conserving the momentum in tangential direction:

$$\left(\frac{V_2}{V_\infty}\right)' \sin(\gamma + \alpha_2') = \left(\frac{V_2}{V_\infty}\right) \sin(\gamma + \alpha_2) \tag{38}$$

This gives the cascade values α_2' and V_2' as shown in Fig. 25. The cascade angle α_2' is obtained from combining equations (37) and (38):

$$\alpha_2' = \gamma - \tan^{-1}\left(\frac{\left(\frac{V_2}{V_\infty}\right) \sin(\gamma + \alpha_2)}{\left(\frac{V_1}{V_\infty}\right) \cos\gamma} \right) \tag{39}$$

After that V_2' is found from equation (38) and the corresponding lift coefficient is evaluated from the usual relation:

$$C_L = \frac{2}{\sigma} \cos\left(\gamma + \frac{\alpha'}{2}\right) \left[\tan\gamma - \tan(\gamma + \alpha_2') \right] \tag{40}$$

This method is applied to the mean section of our impeller. The final result is shown in Fig. 23.

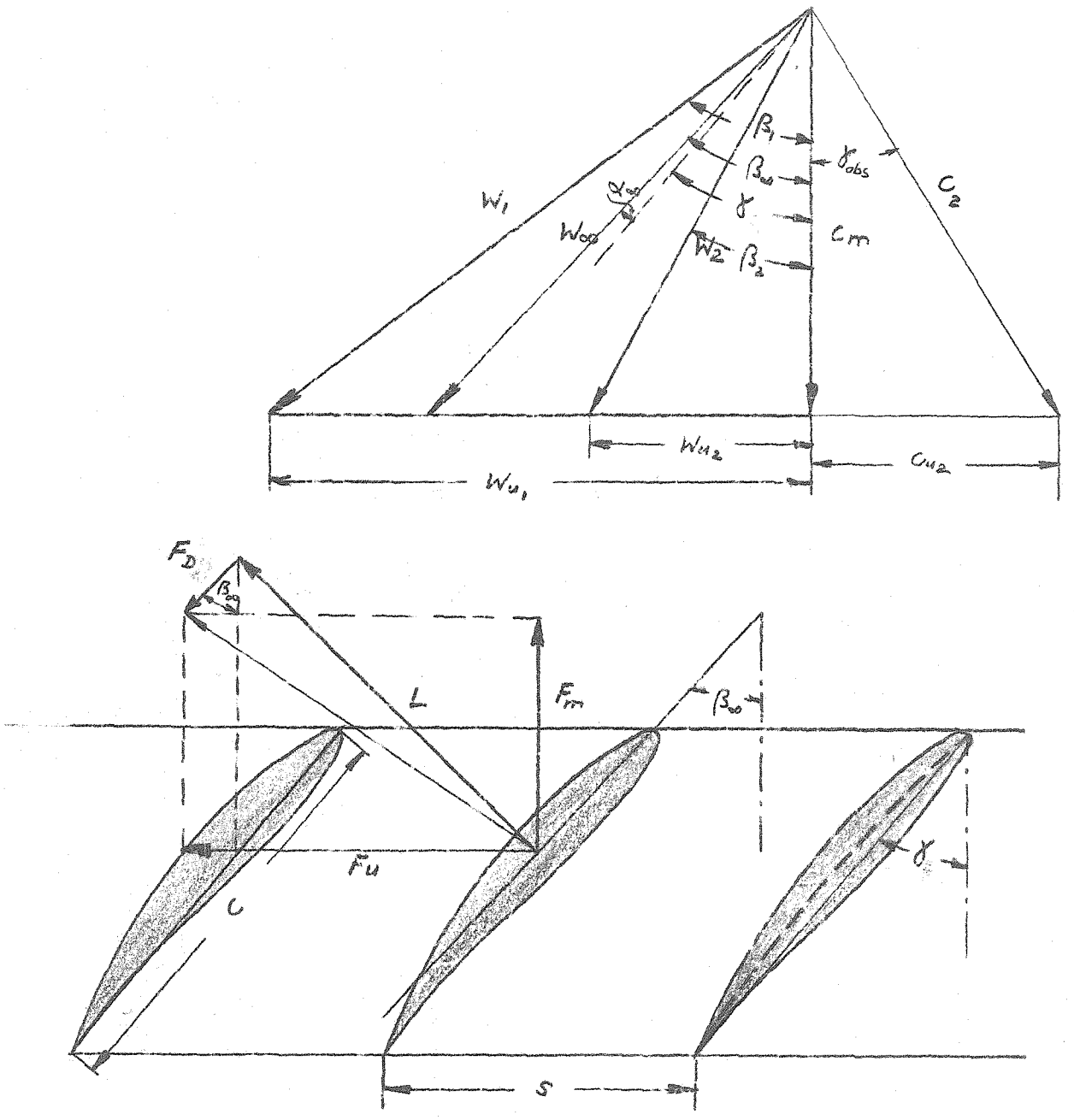

Fig. 1. Definition of cascade geometry.

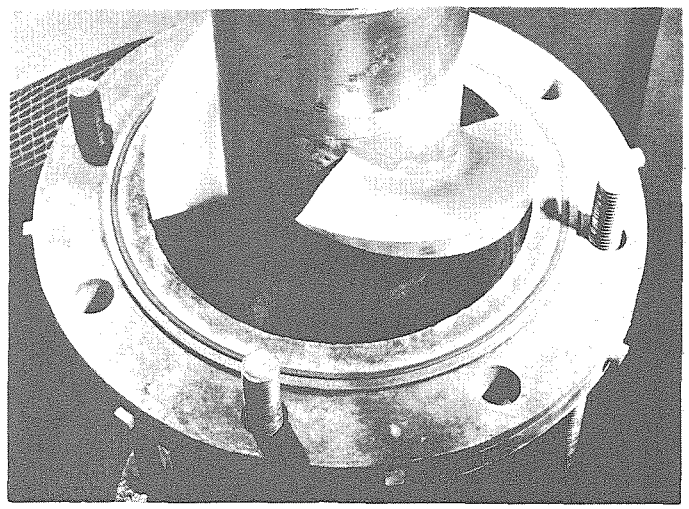

N = 210 RPM $Q = 1.35\phi_{id}$ [cfs] $H = 1.47\psi$ [ft]

$r_1 = 2.25''$ $r_2 = 3.75''$

η	γ	c/s	Ω
0.60	57.6^{o}	0.713	41.6^{o}
0.70	62.8^{o}	0.716	29.1^{o}
0.80	66.4^{o}	0.716	22.0^{o}
0.90	69.1^{o}	0.716	17.3^{o}
1.00	71.4^{o}	0.718	13.9^{o}

Figure 2. Test - Impeller

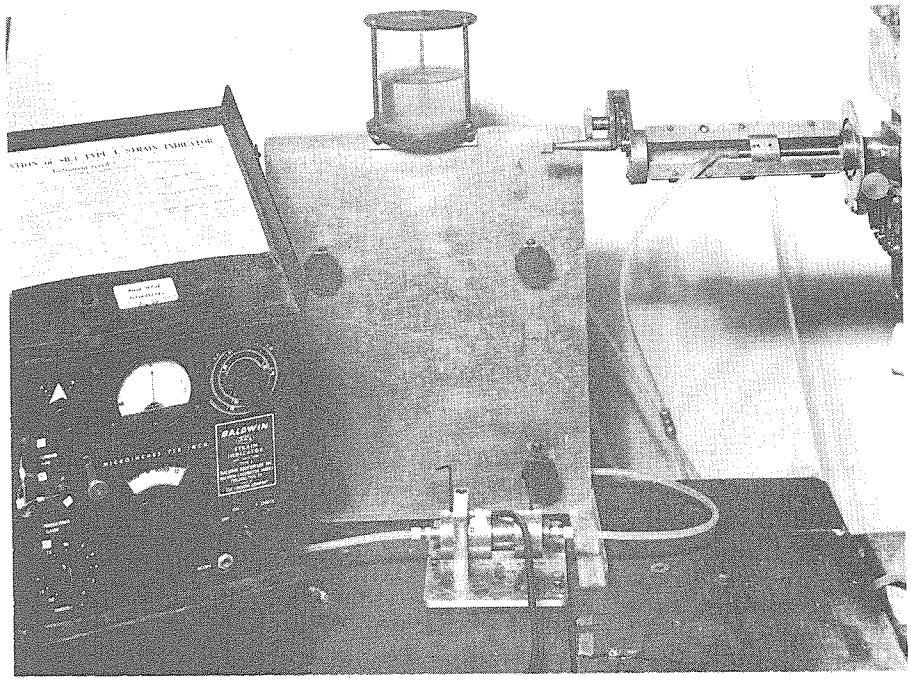

Figure 3. Probeholder and Straingage

(a) wedge probe

(b) static pressure

(c) total pressure

(d) total, boundary-layer probe

Figure 4. Measuring - probes.

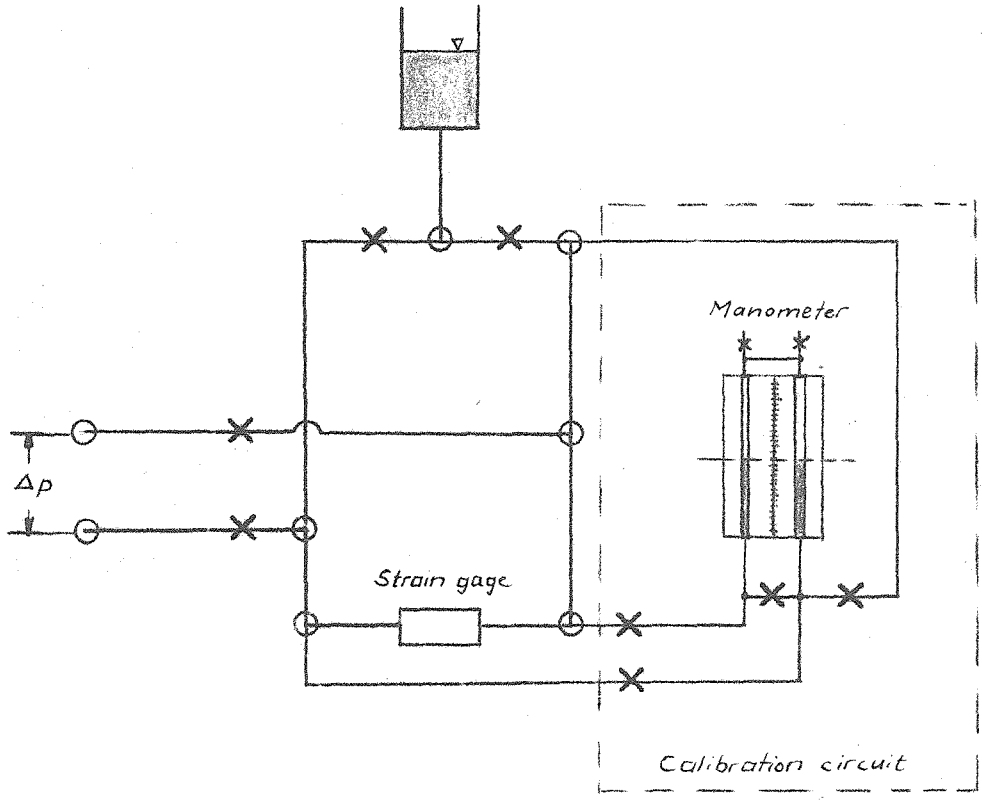

Fig. 5. Strain gage measuring and calibration circuit.

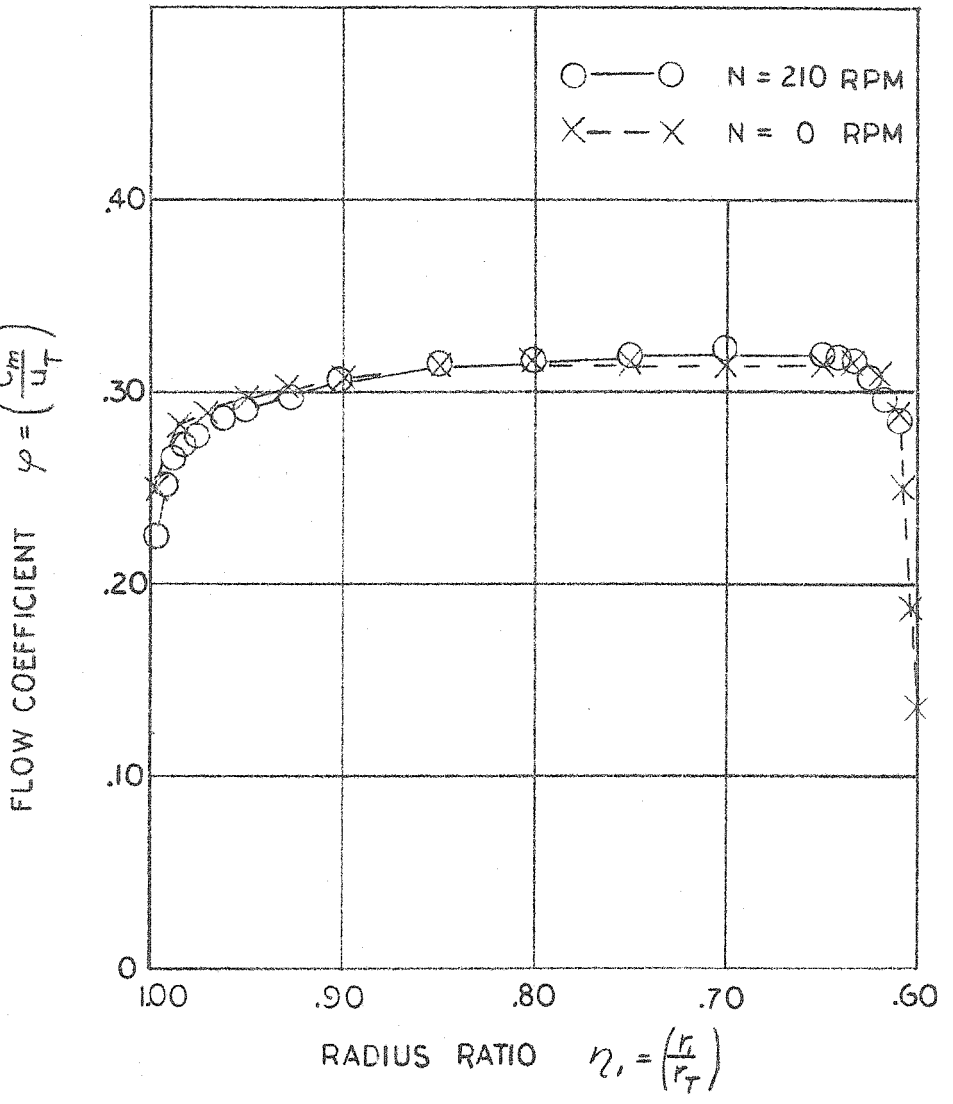

Fig. 6. Upstream velocity profile $\varphi_i = 0.300$.

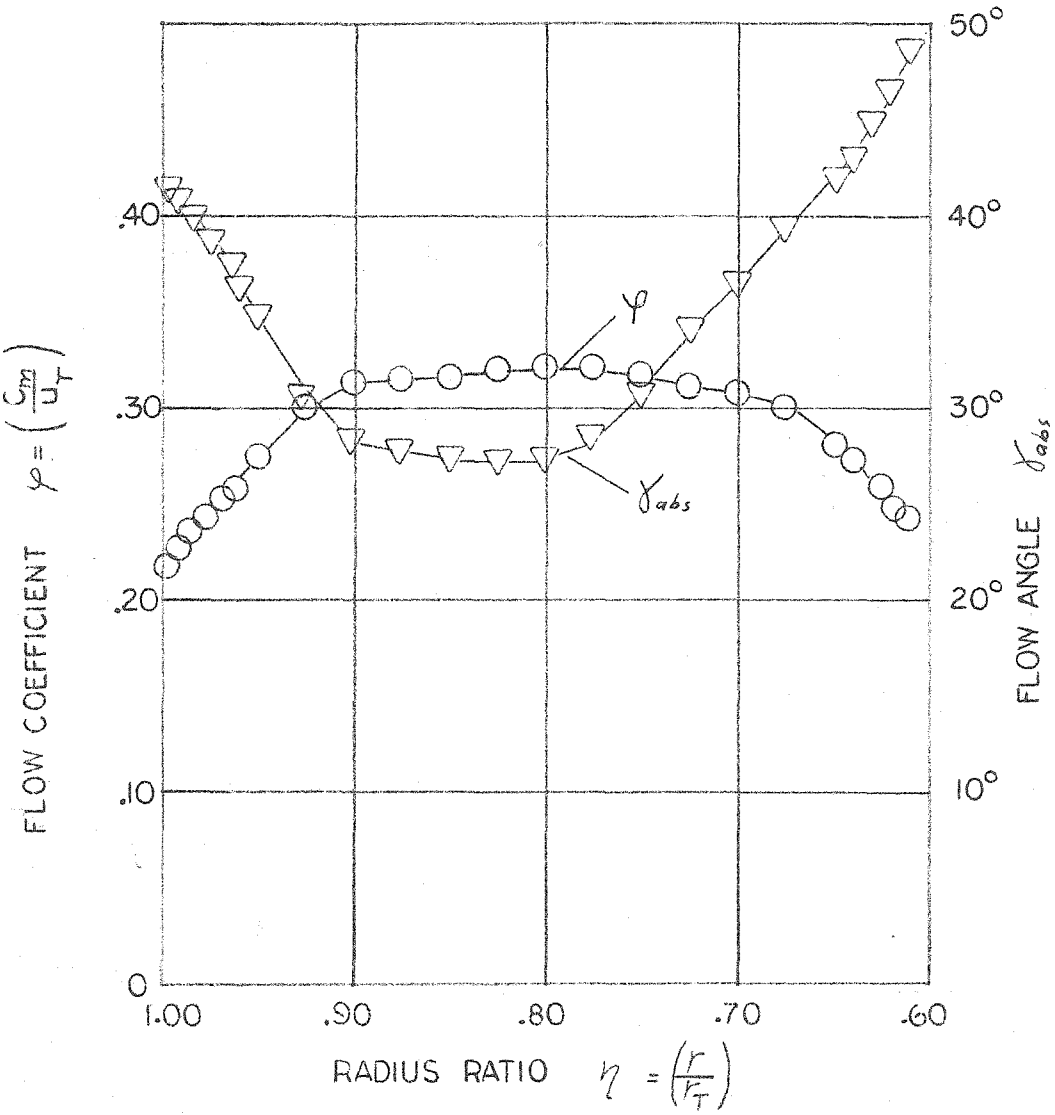

Fig. 7. Downstream velocity profile and distribution of absolute flow angles γ_{abs} (φ_i = .290).

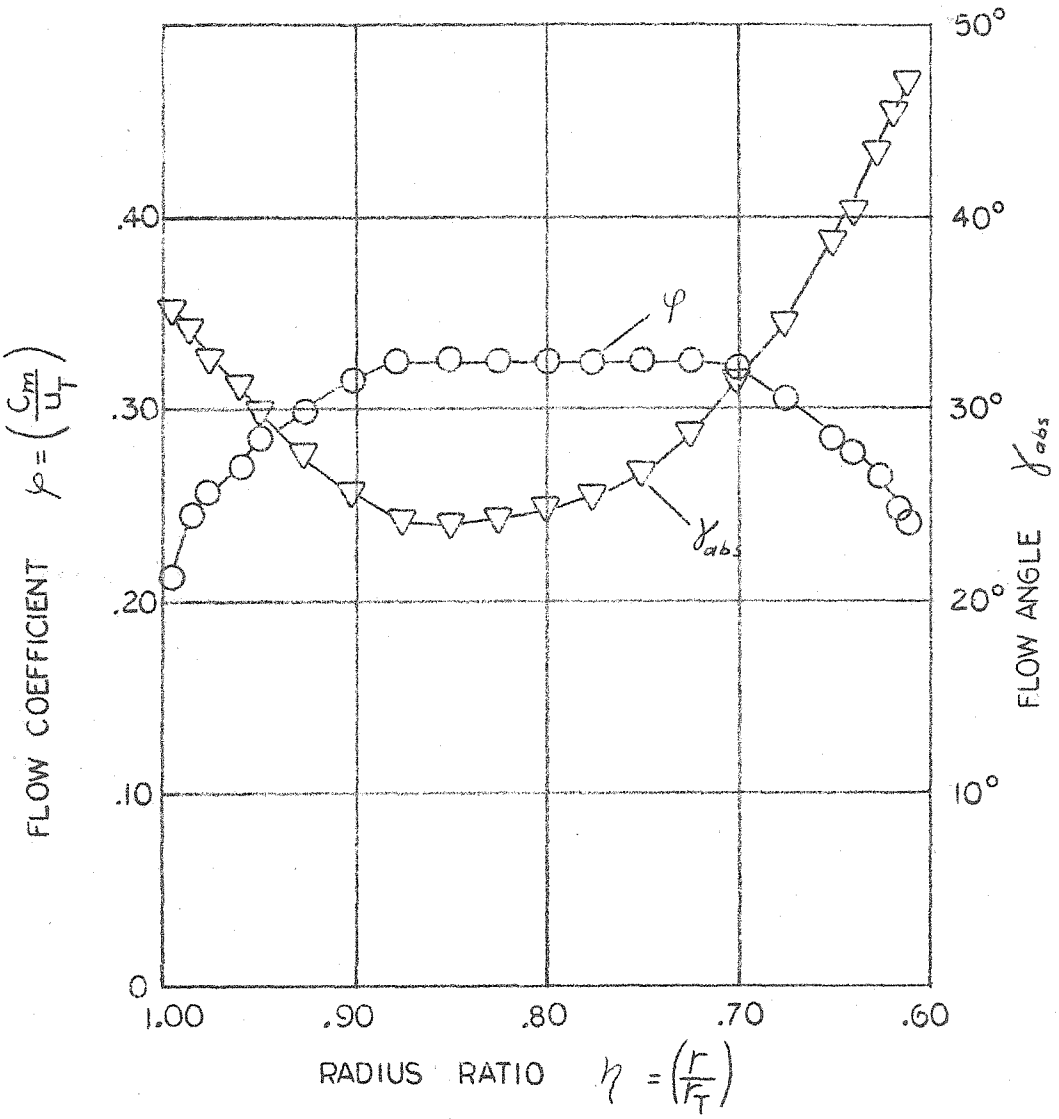

Fig. 8. Downstream velocity profile and distribution of absolute flow angles γ_{abs} ($\varphi_i = 0.300$).

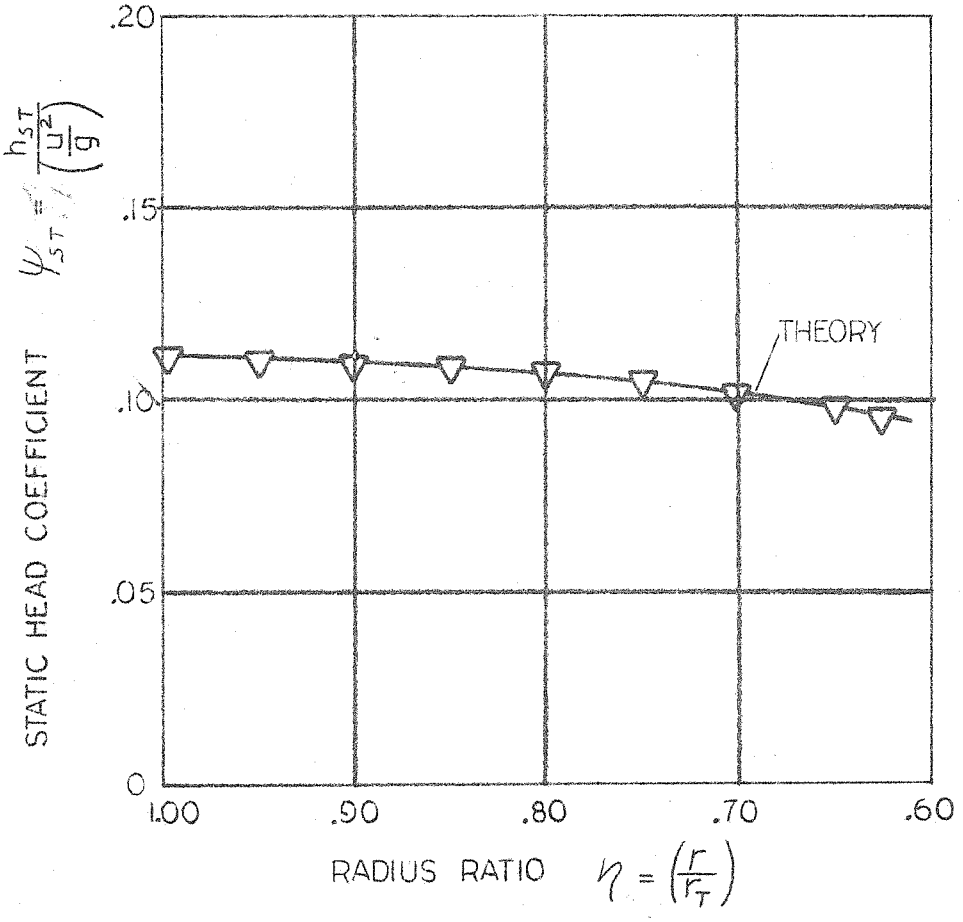

Fig. 9. Comparison of measured and theoretical pressure distribution downstream for $\varphi_i = 0.290$.

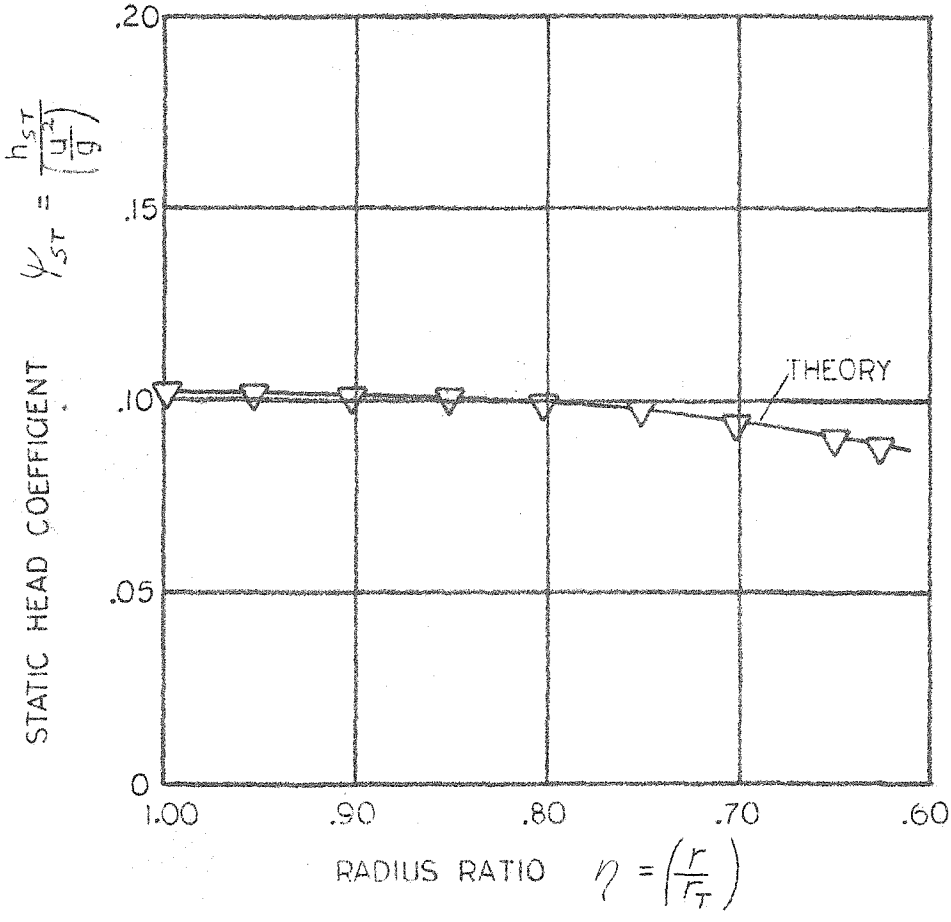

Fig. 10. Comparison of measured and theoretical static pressure distribution downstream for $\varphi_i = 0.300$.

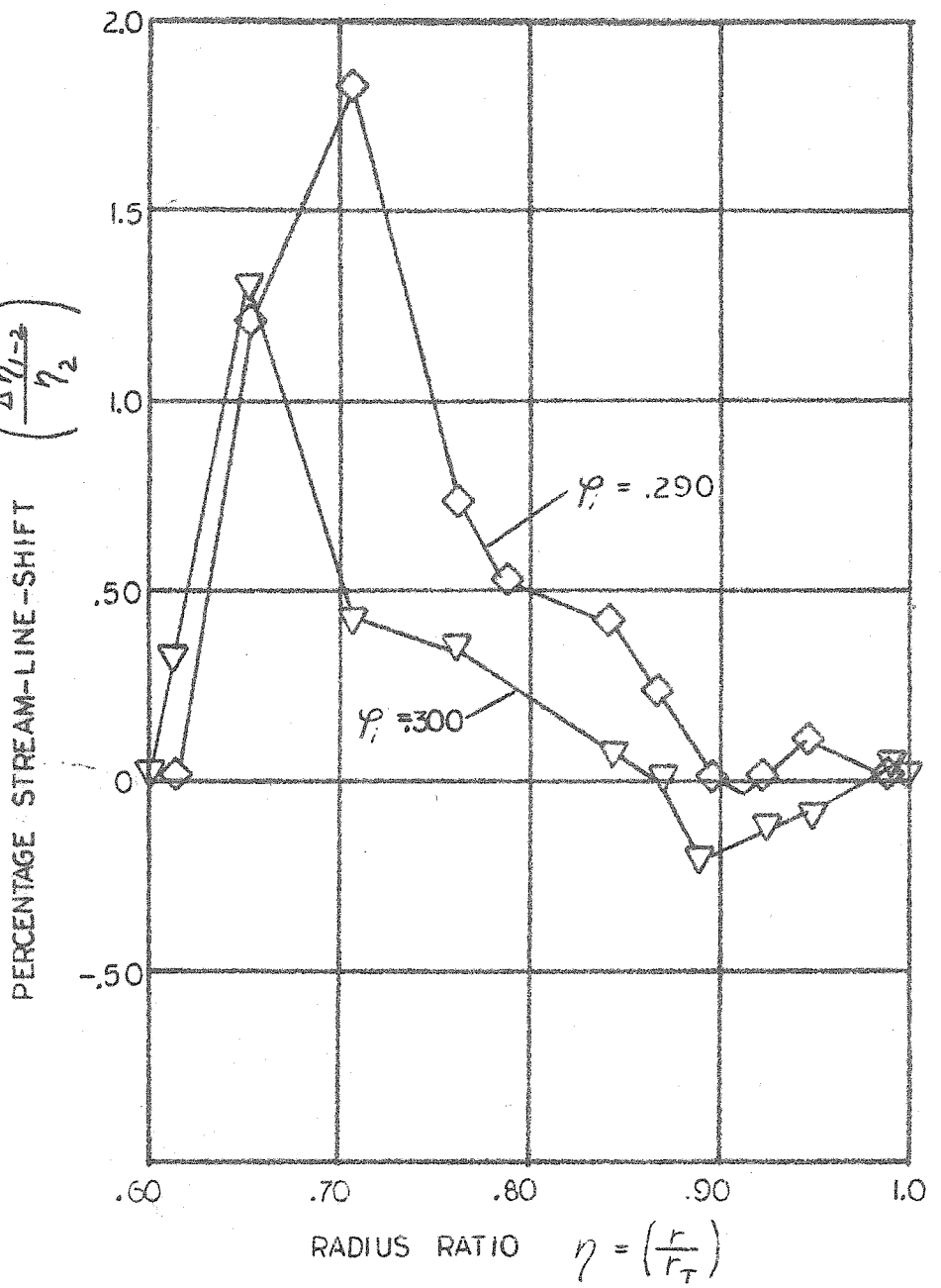

Fig. 11. Measured streamline-shift between measuring stations.

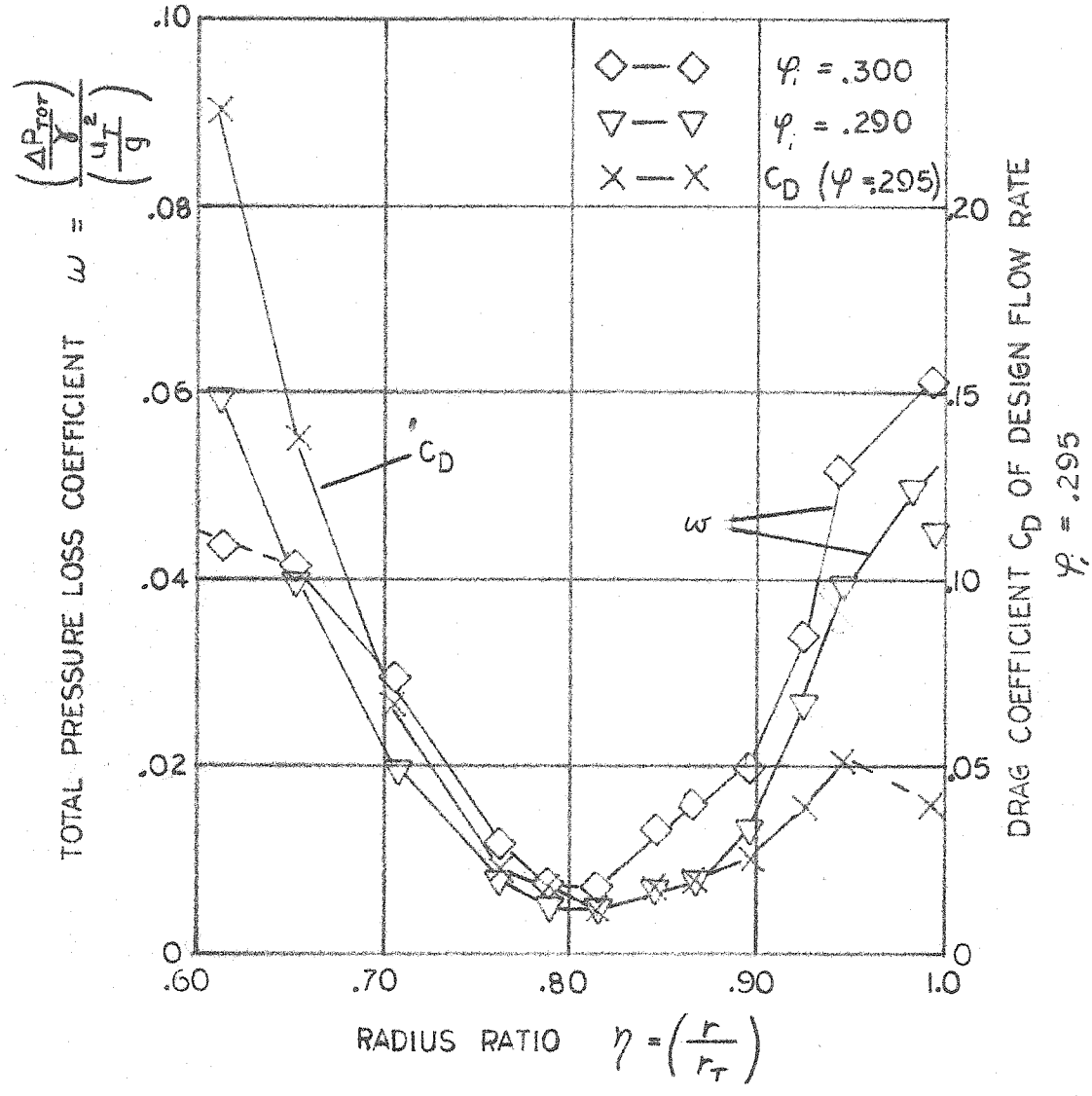

Fig. 12. Measured total pressure loss coefficient and calculated drag coefficients of design-flow rate $\varphi_i = 0.295$.

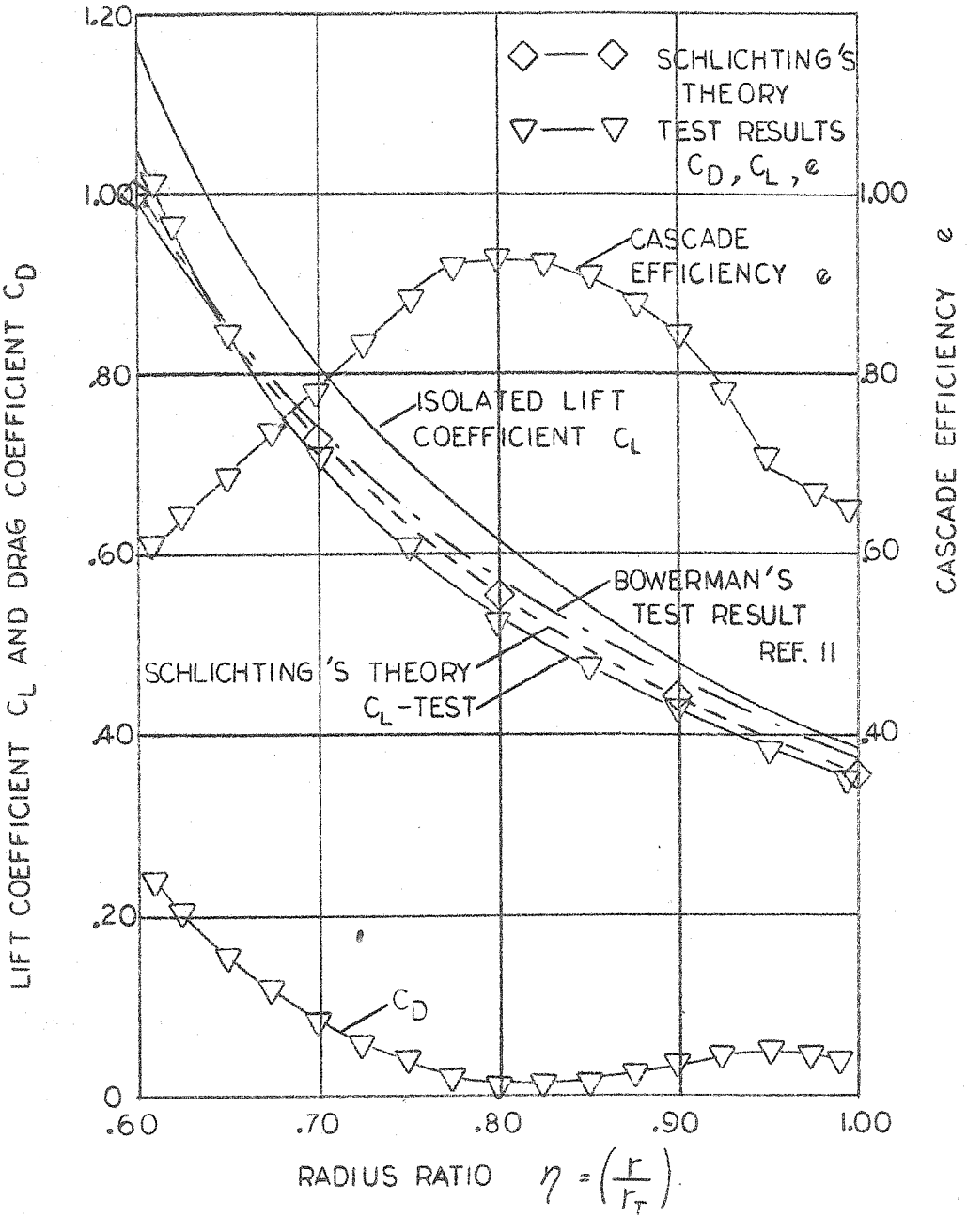

Fig. 13. Comparison of theoretical and measured lift coefficients.

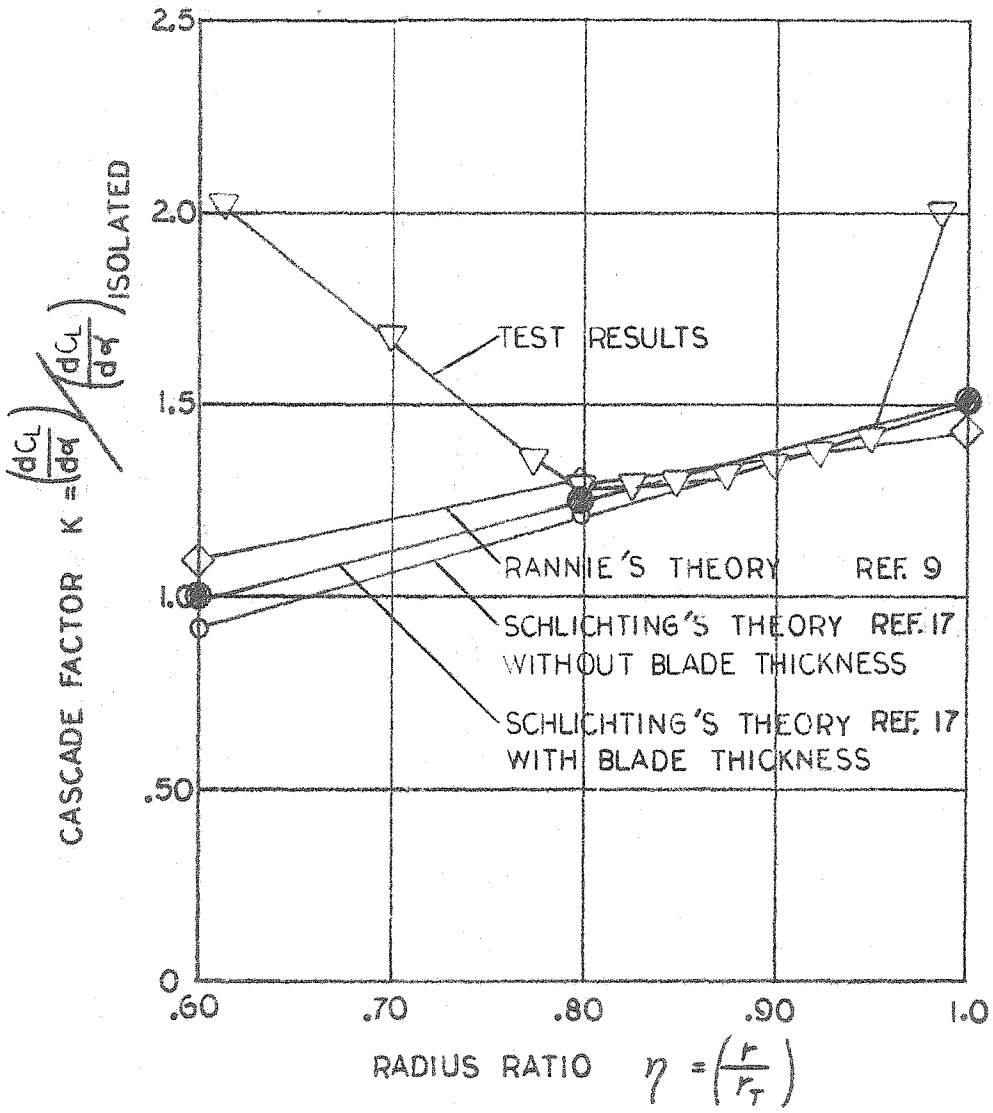

Fig. 14. Comparison of theoretical and measured lift slope parameters.

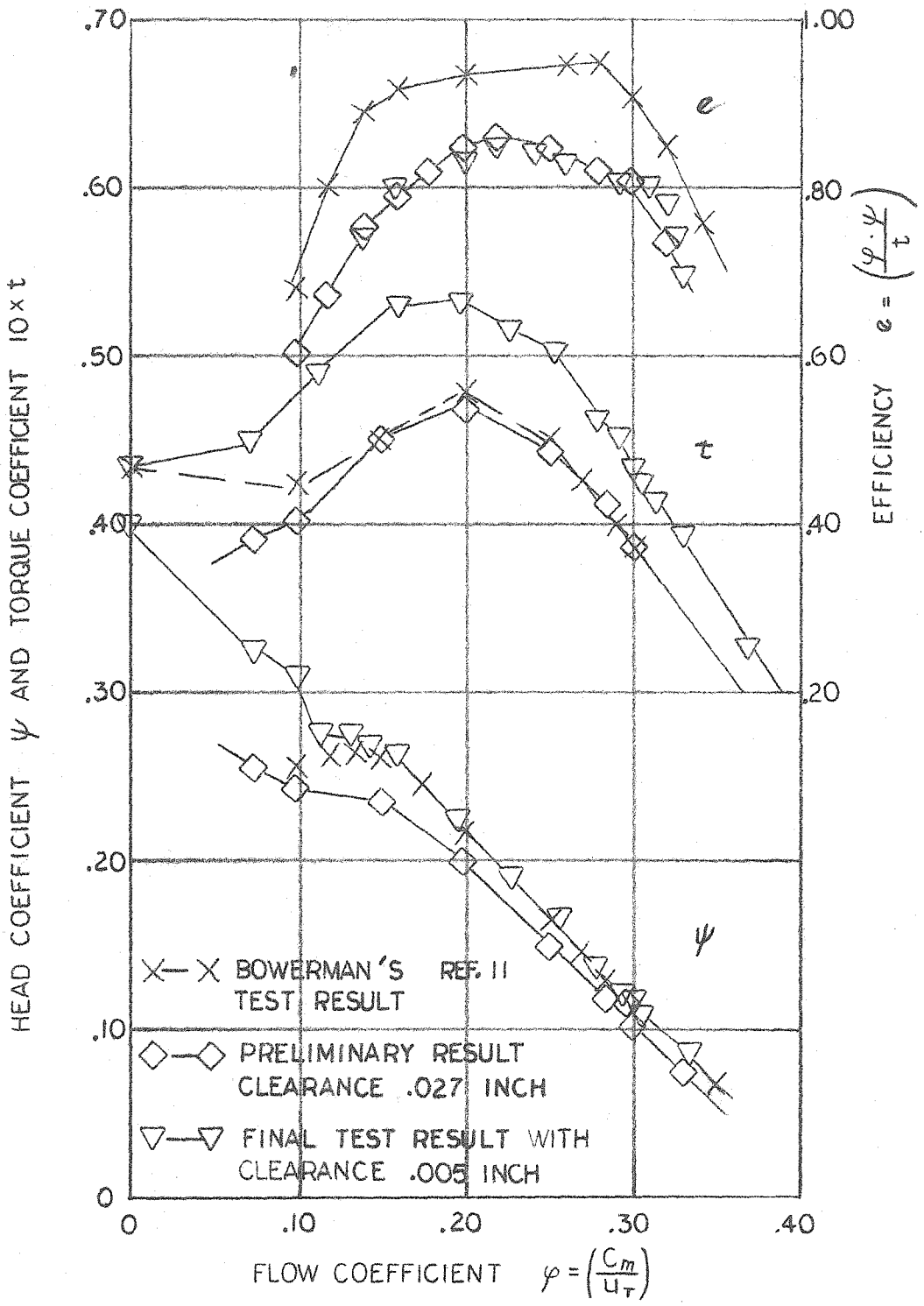

Fig. 15. Performance of mean stream-line.

Comparison of Theoretical Expectations
with and without Thickness Effect as
Percentage from Isolated Airfoil Performance

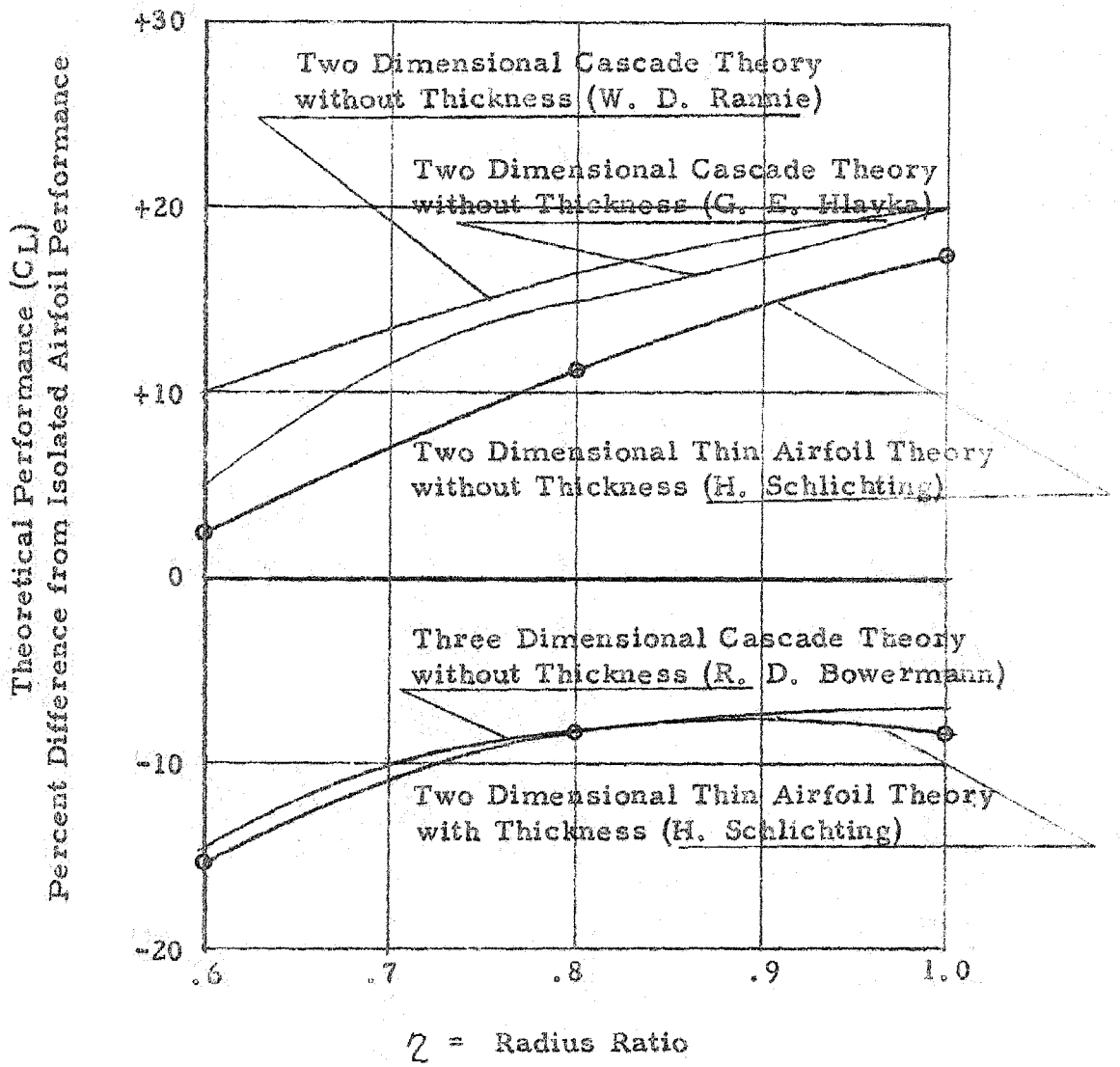

Fig. 16. Comparison of theoretical expectations with and without thickness effect as percentage from isolated airfoil performance.

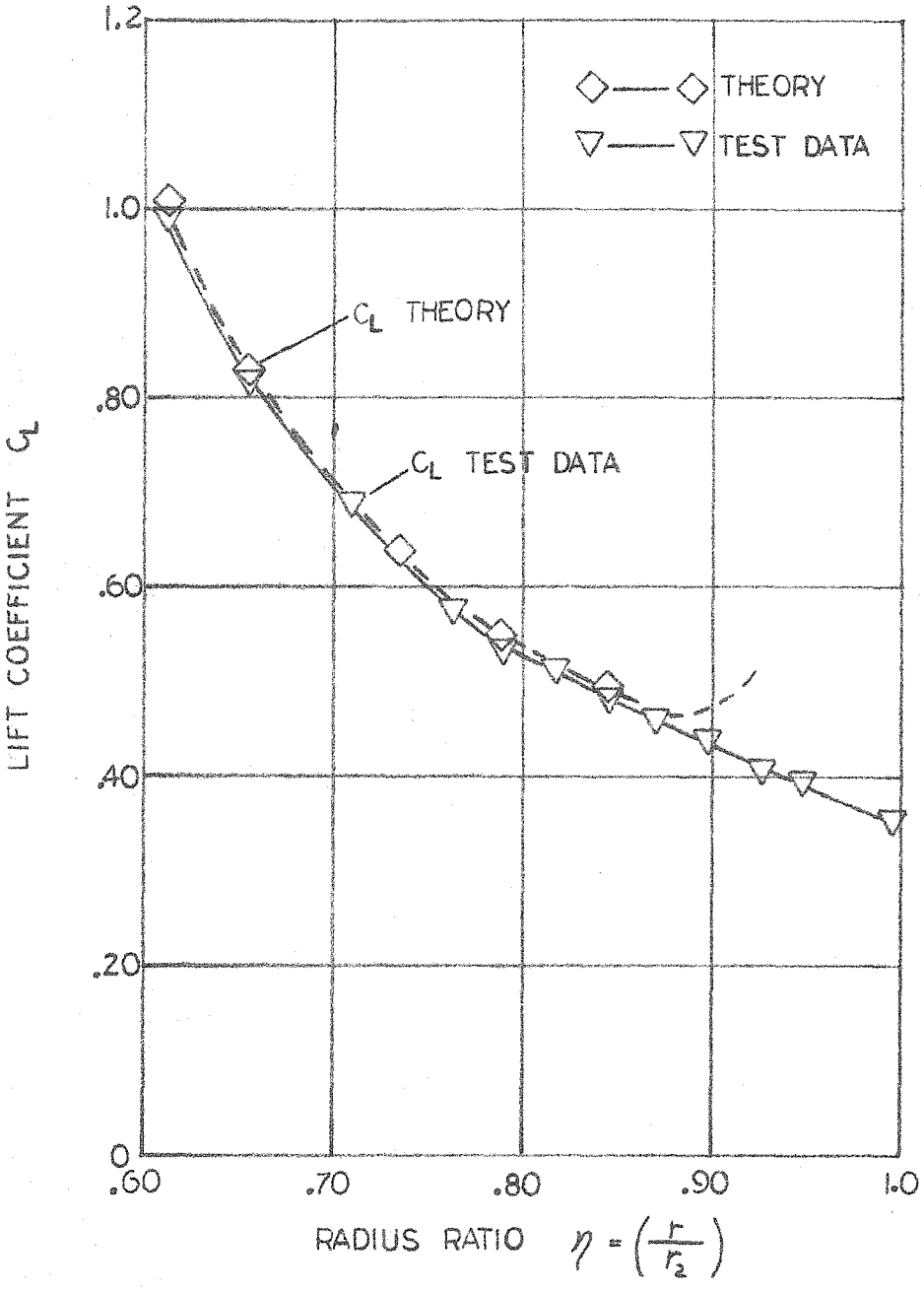

Fig. 17. Comparison of theoretical lift coefficients, corrected according to measured angles of attack, and measured lift coefficients.

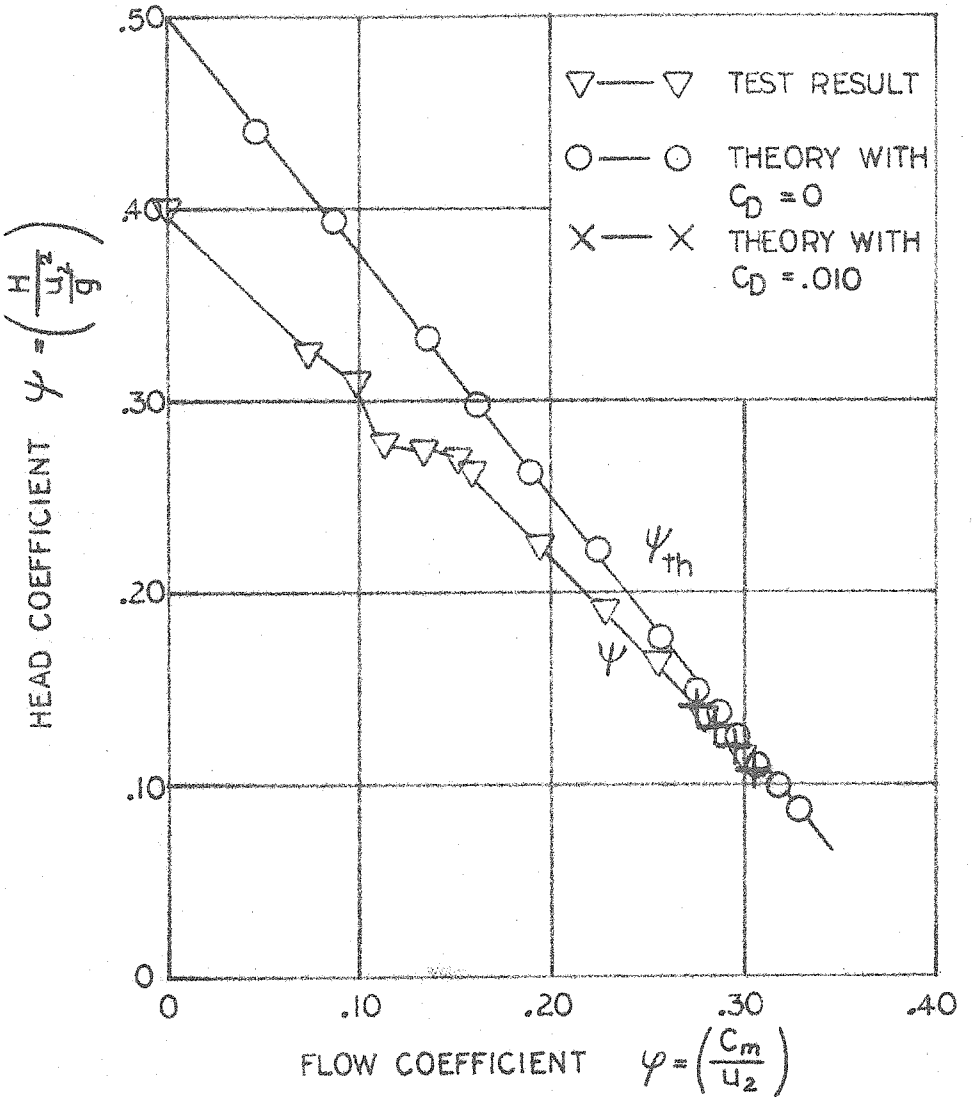

Fig. 18. Theoretical and measured off-design performance of mean stream-line.

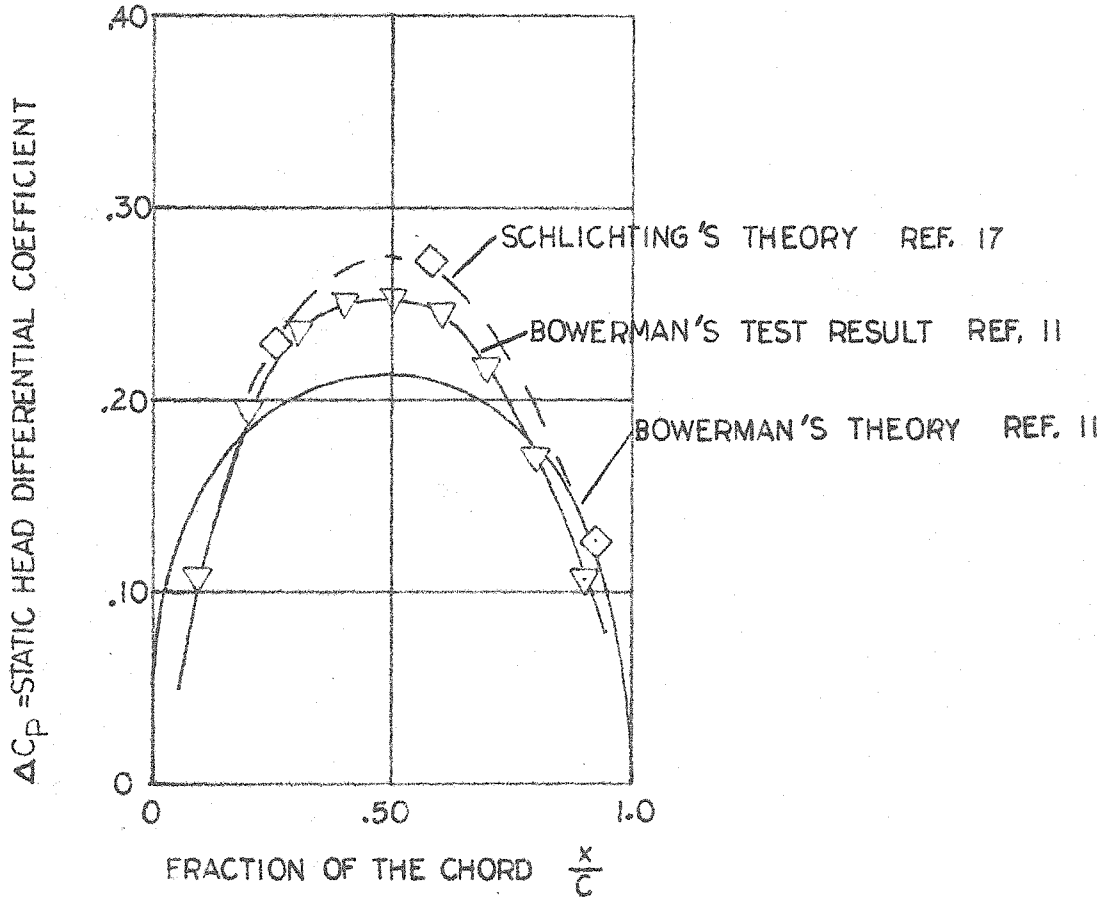

Fig. 19. Comparison of theoretical and measured pressure distribution along the chord of mean radial section ($\varphi_1 = 0.295$).

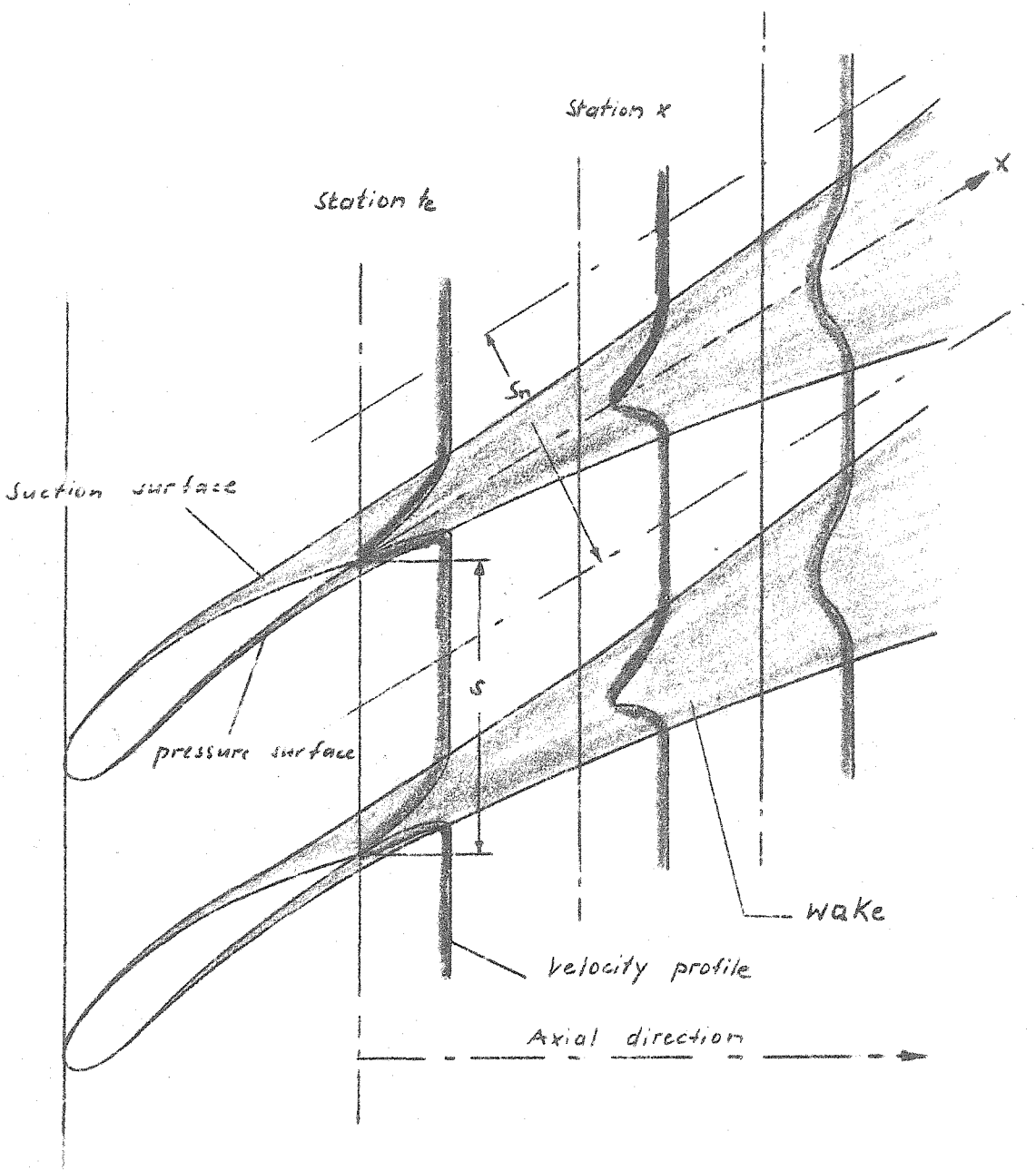

Fig. 20. Model for boundary-layer concept in cascade.

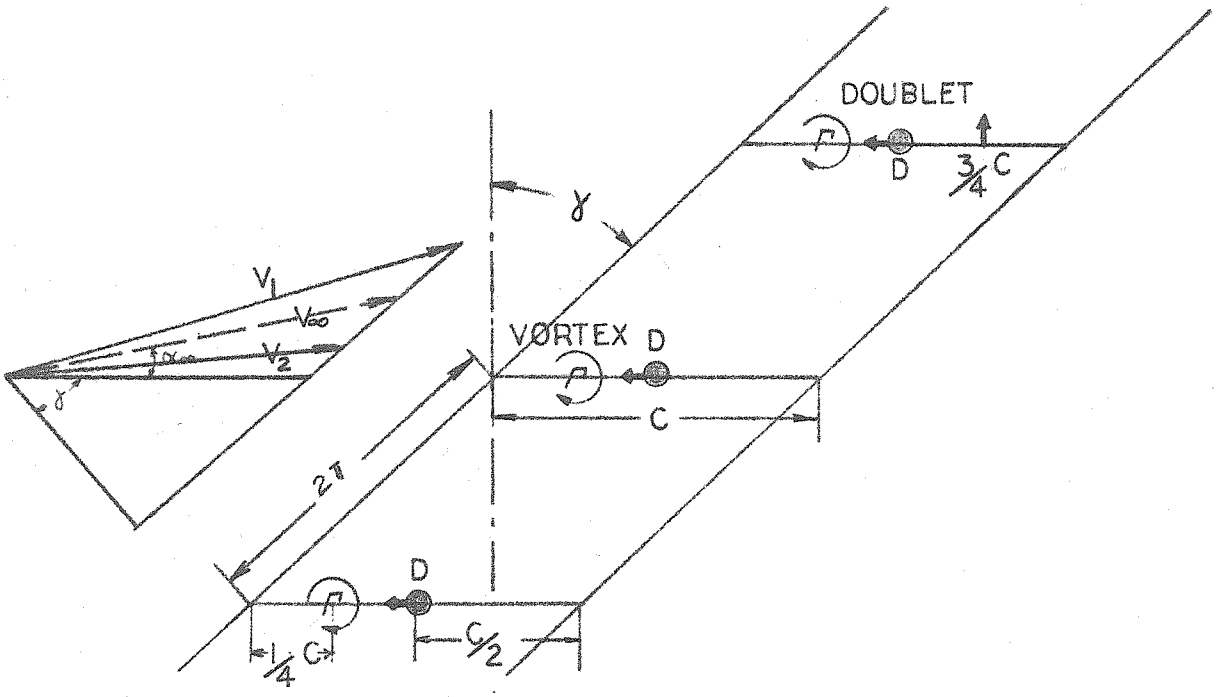

Fig. 21. Two-point method describing thickness effect on cascade flow.

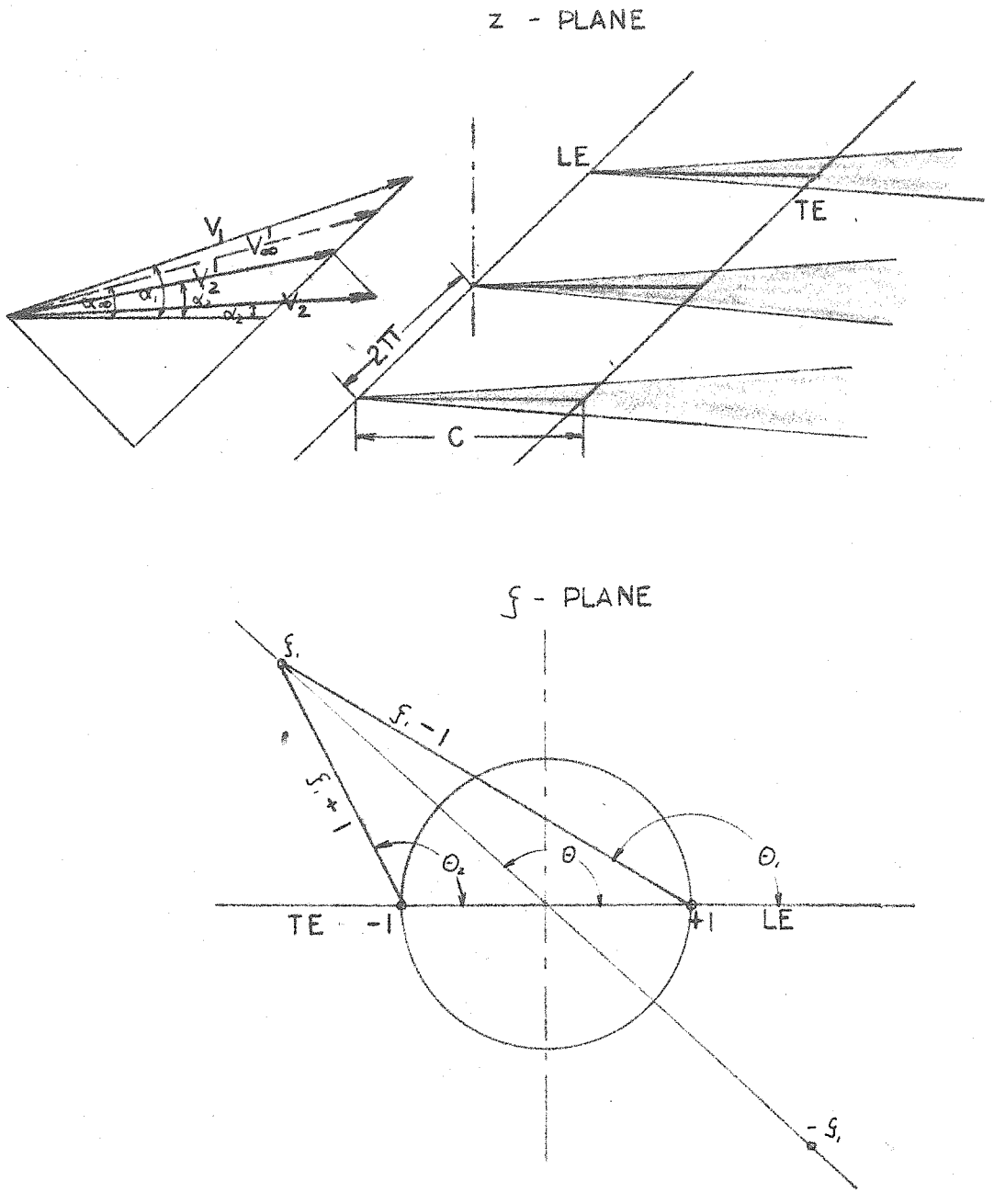

Fig. 22. Cascade and circle plane for calculating the effect of the boundary displacement thickness on the cascade flow.

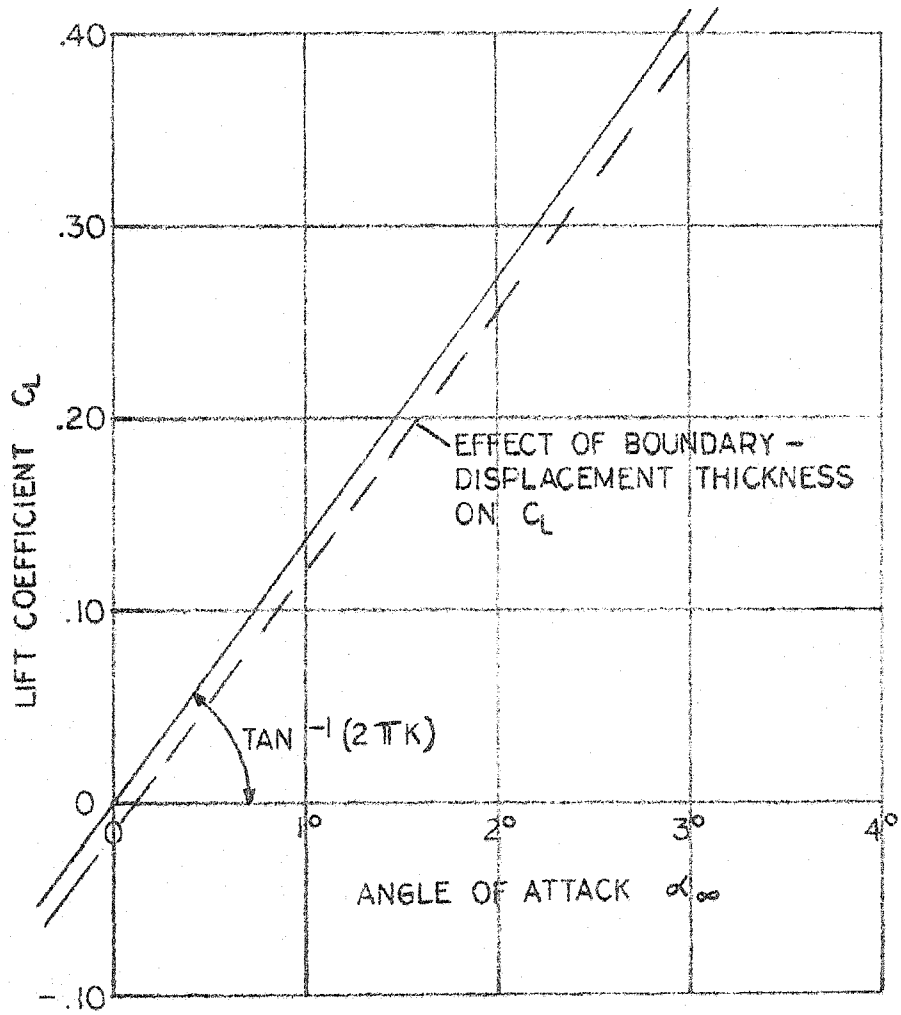

Fig. 23. Effect of the boundary displacement thickness on the cascade flow.